



HAL
open science

Regulation of Solar Wind Electron Temperature Anisotropy by Collisions and Instabilities

Peter H. Yoon, Chadi S. Salem, Kristopher G. Klein, Mihailo M. Martinović, Rodrigo A. López, Jungjoon Seough, Muhammad Sarfraz, Marian Lazar, Shaaban M. Shaaban

► **To cite this version:**

Peter H. Yoon, Chadi S. Salem, Kristopher G. Klein, Mihailo M. Martinović, Rodrigo A. López, et al.. Regulation of Solar Wind Electron Temperature Anisotropy by Collisions and Instabilities. The Astrophysical Journal, 2024, 975, 10.3847/1538-4357/ad7b09 . insu-04853401

HAL Id: insu-04853401

<https://insu.hal.science/insu-04853401v1>

Submitted on 24 Dec 2024

HAL is a multi-disciplinary open access archive for the deposit and dissemination of scientific research documents, whether they are published or not. The documents may come from teaching and research institutions in France or abroad, or from public or private research centers.

L'archive ouverte pluridisciplinaire **HAL**, est destinée au dépôt et à la diffusion de documents scientifiques de niveau recherche, publiés ou non, émanant des établissements d'enseignement et de recherche français ou étrangers, des laboratoires publics ou privés.



Distributed under a Creative Commons Attribution 4.0 International License



Regulation of Solar Wind Electron Temperature Anisotropy by Collisions and Instabilities

Peter H. Yoon¹, Chadi S. Salem², Kristopher G. Klein³, Mihailo M. Martinović^{3,4}, Rodrigo A. López^{5,6}, Jungjoon Seough⁷, Muhammad Sarfraz⁸, Marian Lazar^{9,10}, and Shaaban M. Shaaban¹¹

¹ Institute for Physical Science and Technology, University of Maryland, College Park, MD 20742-2431, USA; yoopn@umd.edu

² Space Sciences Laboratory, University of California, Berkeley, CA 94720, USA

³ Lunar & Planetary Laboratory, University of Arizona, Tucson, AZ 85721-0092, USA

⁴ LESIA, Observatoire de Paris, Meudon, France

⁵ Research Center in the Intersection of Plasma Physics, Matter, and Complexity (P^2mc), Comisión Chilena de Energía Nuclear, Casilla 188-D, Santiago, Chile

⁶ Departamento de Ciencias Físicas, Facultad de Ciencias Exactas, Universidad Andres Bello, Sazié 2212, Santiago 8370136, Chile

⁷ Korea Astronomy and Space Science Institute, Daejeon 34055, Republic of Korea

⁸ Department of Physics, GC University Lahore, Katchery Road, Lahore 54000, Pakistan

⁹ Centre for Mathematical Plasma Astrophysics, Celestijnenlaan 200B, B-3001 Leuven, Belgium

¹⁰ Institut für Theoretische Physik IV, Ruhr-Universität Bochum, D-44780 Bochum, Germany

¹¹ Department of Physics and Materials Sciences, College of Arts and Sciences, Qatar University, 2713 Doha, Qatar

Received 2024 July 24; revised 2024 September 12; accepted 2024 September 12; published 2024 October 29

Abstract

Typical solar wind electrons are modeled as being composed of a dense but less energetic thermal “core” population plus a tenuous but energetic “halo” population with varying degrees of temperature anisotropies for both species. In this paper, we seek a fundamental explanation of how these solar wind core and halo electron temperature anisotropies are regulated by combined effects of collisions and instability excitations. The observed solar wind core/halo electron data in $(\beta_{\parallel}, T_{\perp}/T_{\parallel})$ phase space show that their respective occurrence distributions are confined within an area enclosed by outer boundaries. Here, T_{\perp}/T_{\parallel} is the ratio of perpendicular and parallel temperatures and β_{\parallel} is the ratio of parallel thermal energy to background magnetic field energy. While it is known that the boundary on the high- β_{\parallel} side is constrained by the temperature anisotropy-driven plasma instability threshold conditions, the low- β_{\parallel} boundary remains largely unexplained. The present paper provides a baseline explanation for the low- β_{\parallel} boundary based upon the collisional relaxation process. By combining the instability and collisional dynamics it is shown that the observed distribution of the solar wind electrons in the $(\beta_{\parallel}, T_{\perp}/T_{\parallel})$ phase space is adequately explained, both for the “core” and “halo” components.

Unified Astronomy Thesaurus concepts: [Solar physics \(1476\)](#); [Solar wind \(1534\)](#); [Heliosphere \(711\)](#); [Interplanetary physics \(827\)](#)

Materials only available in the online version of record: animations

1. Introduction

Understanding the physics of solar wind is a contemporary research topic. Ongoing inner heliospheric missions from NASA and ESA, namely Parker Solar Probe (N. J. Fox et al. 2016; S. D. Bale et al. 2023; N. E. Raouafi et al. 2023) and Solar Orbiter (SolO; D. Müller et al. 2020; S. Opie et al. 2022), have unveiled a number of intriguing discoveries (L. P. Chitta et al. 2023). Among the fundamental science questions these missions are exploring is the nature of the evolution of the thermodynamic states of the charged particles that comprise the solar wind—e.g., the protons, electrons, and helium (or alpha) particles. One useful means of studying this evolution is through occurrence distributions—two-dimensional (2D) histograms—of their physical states. A canonical occurrence diagram uses the phase space defined by the parallel plasma beta $\beta_{\parallel,s}$ and the ratio of perpendicular and parallel temperatures (defined with respect to the ambient magnetic field \mathbf{B}), $T_{\perp,s}/T_{\parallel,s}$ (J. C. Kasper et al. 2002, 2003; E. Marsch et al. 2006; S. D. Bale et al. 2009; B. A. Maruca et al. 2011, 2012; J. He et al. 2013; L. Matteini et al. 2013; P. Hellinger &

P. M. Trávníček 2014; C. H. K. Chen et al. 2016; K. G. Klein et al. 2018, 2019, 2021; D. Perrone et al. 2019; J. Huang et al. 2020). Here, $T_{\perp,s}$ and $T_{\parallel,s}$ are perpendicular and parallel temperatures for each species (labeled s). The parallel plasma beta for species s is defined by $\beta_{\parallel,s} = 8\pi n_s T_{\parallel,s} / B^2$, where n_s and B stand for the density for species s and ambient magnetic field intensity, respectively. The data show that the charged-particle distributions in this phase space are confined within an area encompassed by a rhombic-shaped outer boundary. It is well established that the outer boundaries in the high-beta regime are partially defined by various temperature anisotropy instability threshold conditions (S. P. Gary et al. 1997, 2001; E. Marsch et al. 2004; P. Hellinger et al. 2006; L. Matteini et al. 2007; S. M. Shaaban et al. 2017, 2019a; P. H. Yoon 2017; H. Sun et al. 2019, 2020; D. Verscharen et al. 2019; G. Q. Zhao et al. 2019; L. Xiang et al. 2020, 2021; M. M. Martinović et al. 2021), but the boundaries in the low-beta regime are largely unexplained.

A recent paper by the present group of authors (P. H. Yoon et al. 2024) extended the earlier work by S. Vafin et al. (2019), demonstrating that the boundaries associated with the solar wind protons can be explained by a combination of collisional and collective (i.e., instability excitation) relaxations. While S. Vafin et al. (2019) invoked the proton collisional relaxation frequency, ν_{pp} , to show that a certain contour of ν_{pp} , when

parametrized with T_{\perp}/T_{\parallel} and β_{\parallel} , matches the low-beta boundary, P. H. Yoon et al. (2024) carried out the dynamical calculation of collisional relaxation of bi-Maxwellian protons in the low-beta regime. This calculation demonstrated that a hypothetical ensemble of solar wind protons with initially low-beta values undergo collisional relaxation and settle down to the state described by the low-beta outer boundary within a typical transit time between the solar source and the distance of 1 au. Conversely, for high-beta protons, it is the instability excitation and subsequent quasilinear saturation that brings the unstable protons close to the high-beta outer boundary.

In the present paper, we focus on the electrons (Š. Štverák et al. 2008; M. L. Adrian et al. 2016; V. Pierrard et al. 2016; H. Sun et al. 2020). The solar wind electrons are observed to be made of several distinct components, but the simplest description is the two-component model where the electrons comprise dense Maxwellian core electrons and a tenuous but energetic halo electron population (W. C. Feldman et al. 1975; C. S. Salem et al. 2023). Typically, the core and halo electrons are characterized by a finite relative drift, and they also exhibit different degrees of temperature anisotropy in their respective reference frame (L. B. I. Wilson et al. 2019). Moreover, the halo electrons are characterized by a ubiquitous suprathermal population, a feature that is often modeled by a bi-kappa velocity distribution function (V. M. Vasyliunas 1968; M. Maksimovic et al. 1997; C. S. Salem et al. 2023). In the present study, we ignore the relative drift and also model the halo electron population by a bi-Maxwellian velocity distribution, for the sake of simplicity, focusing on the temperature anisotropies of bi-Maxwellian core and halo electrons. Here, we note that the temperature anisotropy is the dominant source of free energy, and thus understanding the behavior of temperature relaxation is an essential first step to tackling the issue of relaxation of relative drift. Although it is generally assumed that the solar wind near 1 au is largely collision-free, the cumulative effects of binary collisions, known as the collisional age effect, can be important (Š. Štverák et al. 2008; P. Hellinger & P. M. Trávníček 2014; J. C. Kasper et al. 2017), particularly for the electrons (C. S. Salem et al. 2003). We will extend our earlier analysis for the protons (P. H. Yoon et al. 2024) and analyze the collisional and collective relaxation processes for the core and halo electrons.

The organization of this paper is as follows: In Section 2, we discuss the problem of temperature anisotropy relaxation processes by collisions in the low-beta regime. Section 3 is devoted to the discussion of anisotropic temperature relaxation by instability excitation and subsequent quasilinear saturation in the high-beta regime. Section 4 summarizes the findings.

2. Collisional Temperature Relaxation for Core–Halo Electron System

The equations that describe the relaxation of anisotropic temperatures by collisional processes are presented below. The derivation can be found in Appendix A, and these equations pertain to a plasma made of the background protons and two distinct electron components, the core and halo populations. The core (*c*) electrons are characterized by low energy but dense population with distinct bi-Maxwellian temperatures, $T_{\perp c}$ and $T_{\parallel c}$, while the halo (*h*) electrons are tenuous but more energetic, with the bi-Maxwellian temperatures, $T_{\perp h}$ and $T_{\parallel h}$, which are substantially higher than those of the core electrons. Admittedly, it is more realistic to model the halo electrons by a

bi-Kappa distribution, but we nevertheless adopt a bi-Maxwellian model to simplify the analysis. The protons (*p*) are considered as a single species. The protons and core–halo electrons are assumed to satisfy the charge neutrality condition, or equivalently, the density conservation, $n_p = n_c + n_h$, where n_p , n_c , and n_h denote the proton, core, and halo electron densities, respectively. As noted, we ignore the relative drift between the core and halo electrons, or any drifts between the electrons and protons. The relative drifts are important for the heat flux, but as our focus is on explaining the solar wind electron occurrence distribution in $(\beta_{\parallel}, T_{\perp}/T_{\parallel})$ phase space, our main emphasis will be on the anisotropic temperatures. Upon writing out the collisional relaxation Equation (A7) for each species, $a, b = c, h, p$, we arrive at

$$\frac{dT_{\perp c}}{dt} = \nu_{cc}(T_{\parallel c} - T_{\perp c}) + \frac{n_h}{n} \nu_{ch}(T_{\perp h} - T_{\perp c}) + \nu_{cp}(T_{\perp p} - T_{\perp c}), \quad (1a)$$

$$\frac{dT_{\parallel c}}{dt} = 2\nu_{cc}(T_{\perp c} - T_{\parallel c}) + \frac{n_h}{n} \nu_{ch}(T_{\parallel h} - T_{\parallel c}) + \nu_{cp}(T_{\parallel p} - T_{\parallel c}), \quad (1b)$$

$$\frac{dT_{\perp h}}{dt} = \nu_{hh}(T_{\parallel h} - T_{\perp h}) + \frac{n_c}{n} \nu_{ch}(T_{\perp c} - T_{\perp h}) + \nu_{hp}(T_{\perp p} - T_{\perp h}), \quad (1c)$$

$$\frac{dT_{\parallel h}}{dt} = 2\nu_{hh}(T_{\perp h} - T_{\parallel h}) + \frac{n_c}{n} \nu_{ch}(T_{\parallel c} - T_{\parallel h}) + \nu_{hp}(T_{\parallel p} - T_{\parallel h}), \quad (1d)$$

$$\frac{dT_{\perp p}}{dt} = \nu_{pp}(T_{\parallel p} - T_{\perp p}) + \frac{n_c}{n} \nu_{cp}(T_{\perp c} - T_{\perp p}) + \frac{n_h}{n} \nu_{hp}(T_{\perp h} - T_{\perp p}), \quad (1e)$$

$$\frac{dT_{\parallel p}}{dt} = 2\nu_{pp}(T_{\perp p} - T_{\parallel p}) + \frac{n_c}{n} \nu_{cp}(T_{\parallel c} - T_{\parallel p}) + \frac{n_h}{n} \nu_{hp}(T_{\parallel h} - T_{\parallel p}). \quad (1f)$$

The various collisional relaxation frequencies are defined by

$$\nu_{cc} = \sqrt{\frac{m_p}{m_e}} \sqrt{\frac{\pi}{m_p}} \frac{8ne^4 \ln \Lambda}{15} \times \left(\frac{n_c/n + \sqrt{2}}{T_{\parallel c}^{3/2}} + \frac{\sqrt{2}(n_h/n)}{(T_{\parallel c} + T_{\parallel h})^{3/2}} \right), \quad (2a)$$

$$\nu_{hh} = \sqrt{\frac{m_p}{m_e}} \sqrt{\frac{\pi}{m_p}} \frac{8ne^4 \ln \Lambda}{15} \times \left(\frac{n_h/n + \sqrt{2}}{T_{\parallel h}^{3/2}} + \frac{\sqrt{2}(n_c/n)}{(T_{\parallel c} + T_{\parallel h})^{3/2}} \right), \quad (2b)$$

$$\nu_{ch} = \sqrt{\frac{m_p}{m_e}} \sqrt{\frac{2\pi}{m_p}} \frac{8ne^4 \ln \Lambda}{3(T_{\parallel c} + T_{\parallel h})^{3/2}}, \quad (2c)$$

$$\nu_{pp} = \sqrt{\frac{\pi}{m_p}} \frac{8ne^4 \ln \Lambda}{15T_{\parallel p}^{3/2}}, \quad (2d)$$

$$\nu_{cp} = \sqrt{\frac{m_e}{m_p}} \sqrt{\frac{2\pi}{m_p}} \frac{8ne^4 \ln\Lambda}{3T_{\parallel c}^{3/2}}, \quad (2e)$$

$$\nu_{hp} = \sqrt{\frac{m_e}{m_p}} \sqrt{\frac{2\pi}{m_p}} \frac{8ne^4 \ln\Lambda}{3T_{\parallel h}^{3/2}}, \quad (2f)$$

and these expressions follow from the detailed manipulations of Equation (A7). Equations (1a) and (1b) describe the relaxation of anisotropic core electron temperatures by collisions among themselves (the first terms on the right-hand side dictated by ν_{cc}), by collisions with the halo electrons (the second terms associated with ν_{ch}), and through collisions with the protons (the third terms related to ν_{cp}). Similarly, Equations (1c) and (1d) describe the temperature relaxation of halo electrons with each term on the right-hand side specifying different collisional processes, that is, the first terms on the right-hand side describing the self collisions among the halo electrons (ν_{hh}), the second terms describing the core–halo collision (ν_{ch}), and the third terms depicting the halo–proton collision (ν_{hp}). Equations (1e) and (1f) likewise depict the collisional relaxation of proton temperatures, with each term providing the details of different collisional processes, namely, the proton–proton collisions (ν_{pp}), proton–core (ν_{cp}), and proton–halo collisions (ν_{hp}). In the above m_p and m_e denote the proton and electron masses, respectively, e is the unit electric charge, and Λ is defined by $\Lambda = 4\pi n\lambda_D^3$, where $n = n_p = n_c + n_h$ and $\lambda_D^3 = T_e^{3/2}/(4\pi ne^2)^{3/2}$. Here, T_e represents the total electron temperature

$$T_e = \frac{1}{3} \left(\frac{n_c}{n} (2T_{\perp c} + T_{\parallel c}) + \frac{n_h}{n} (2T_{\perp h} + T_{\parallel h}) \right), \quad (3)$$

and λ_D corresponds to the Debye length. In Equations (2a)–(2c), it is seen that the core and halo parallel temperatures are coupled through the definitions of collisional relaxation frequencies.

Following our previous paper (P. H. Yoon et al. 2024), we normalize the time variable with respect to the proton gyrofrequency, $\Omega_p = eB/m_p c$, where c is the speed of light. One would think that the electron time normalization would be more natural for the electron physics, but our purpose here is to deliberately choose the same normalization scheme as in our previous paper so that a direct comparison can be made. The dimensionless temperatures are expressed via plasma betas, the ratio of thermal to magnetic field energy densities. The proton-to-electron mass ratio is denoted by $M = m_p/m_e$. The ratio of halo electron density to the total density is defined by $\delta = n_h/n$. We also normalize the various collision frequencies by the proton gyrofrequency. With this normalization convention all the dimensionless physical quantities that pertain to the present paper can be directly compared with the same quantities and expressions found in our previous paper (P. H. Yoon et al. 2024)

$$\begin{aligned} \tau &= \Omega_p t, & M &= \frac{m_p}{m_e} = 1836, \\ \beta_{\perp, \parallel a} &= \frac{8\pi n_a T_{\perp, \parallel a}}{B^2}, & \bar{\nu}_{ab} &= \frac{\nu_{ab}}{\Omega_p}. \end{aligned} \quad (4)$$

Under the present normalization convention, the same two dimensionless parameters that were introduced in our previous

paper (P. H. Yoon et al. 2024) emerge as the main quantities that characterize the strength of collisional effects

$$\begin{aligned} g &= \frac{\sqrt{2}}{\pi^{3/2}} \frac{1}{n(c/\omega_{pp})^3} \frac{c^4}{v_A^4} = 7.76 \times 10^{-27} \frac{n_{[\text{pcc}]^{5/2}}}{B_{[\text{Gauss}]^4}}, \\ \ln \Lambda &= \ln(4\pi n\lambda_D^3) = \ln \frac{5.16 \times 10^9 T_{[\text{eV}]^{3/2}}}{n_{[\text{pcc}]^{1/2}}, \end{aligned} \quad (5)$$

where $T_{[\text{eV}]}$ represents a reference electron temperature, given in electron volts, $n_{[\text{pcc}]}$ is the background plasma density, given in units of number of particles per cubic centimeter, and $B_{[\text{Gauss}]}$ is the magnetic field intensity, given in Gauss, respectively. In Equation (5), $\omega_{pp} = (4\pi ne^2/m_p)^{1/2}$ and $v_A = B/(4\pi nm_p)^{1/2}$ represent the proton plasma oscillation frequency and the Alfvén speed, respectively. The quantity g is related to the inverse of the number of plasma particles in a sphere with the radius equal to the proton inertial length, $L_p = c/\omega_{pp}$. Thus, if the number of particles in this sphere is infinite, $N = nL_p^3 \rightarrow \infty$, then $g \rightarrow 0$, and the plasma is perfectly collision-free. For a finite value of g , however, the binary collisions among plasma particles cannot be ignored. In general, g must be sufficiently small for a plasma. The quantity $\ln\Lambda$ is the familiar Coulomb logarithm.

In terms of the normalized quantities, the set of equations that describe the collisional relaxation of anisotropic temperatures, namely Equations (1a)–(2f), can be re-expressed as

$$\begin{aligned} \frac{d\beta_{\perp c}}{d\tau} &= \bar{\nu}_{cc}(\beta_{\parallel c} - \beta_{\perp c}) + (1 - \delta)\bar{\nu}_{ch}(\beta_{\perp h} - \beta_{\perp c}) \\ &+ (1 - \delta)\bar{\nu}_{cp}(\beta_{\perp p} - \beta_{\perp c}), \end{aligned} \quad (6a)$$

$$\begin{aligned} \frac{d\beta_{\parallel c}}{d\tau} &= 2\bar{\nu}_{cc}(\beta_{\perp c} - \beta_{\parallel c}) + (1 - \delta)\bar{\nu}_{ch}(\beta_{\parallel h} - \beta_{\parallel c}) \\ &+ (1 - \delta)\bar{\nu}_{cp}(\beta_{\parallel p} - \beta_{\parallel c}), \end{aligned} \quad (6b)$$

$$\begin{aligned} \frac{d\beta_{\perp h}}{d\tau} &= \bar{\nu}_{hh}(\beta_{\parallel h} - \beta_{\perp h}) + \delta\bar{\nu}_{ch}(\beta_{\perp c} - \beta_{\perp h}) \\ &+ \delta\bar{\nu}_{hp}(\beta_{\perp p} - \beta_{\perp h}), \end{aligned} \quad (6c)$$

$$\begin{aligned} \frac{d\beta_{\parallel h}}{d\tau} &= 2\bar{\nu}_{hh}(\beta_{\perp h} - \beta_{\parallel h}) + \delta\bar{\nu}_{ch}(\beta_{\parallel c} - \beta_{\parallel h}) \\ &+ \delta\bar{\nu}_{hp}(\beta_{\parallel p} - \beta_{\parallel h}), \end{aligned} \quad (6d)$$

$$\begin{aligned} \frac{d\beta_{\perp p}}{d\tau} &= \bar{\nu}_{pp}(\beta_{\parallel p} - \beta_{\perp p}) + (1 - \delta)\bar{\nu}_{cp}(\beta_{\perp c} - \beta_{\perp p}) \\ &+ \delta\bar{\nu}_{hp}(\beta_{\perp h} - \beta_{\perp p}), \end{aligned} \quad (6e)$$

$$\begin{aligned} \frac{d\beta_{\parallel p}}{d\tau} &= 2\bar{\nu}_{pp}(\beta_{\perp p} - \beta_{\parallel p}) + (1 - \delta)\bar{\nu}_{cp}(\beta_{\parallel c} - \beta_{\parallel p}) \\ &+ \delta\bar{\nu}_{hp}(\beta_{\parallel h} - \beta_{\parallel p}), \end{aligned} \quad (6f)$$

$$\begin{aligned} \bar{\nu}_{cc} &= \frac{\sqrt{M} g \ln\Lambda'}{15} \left(\frac{1 - \delta + \sqrt{2}}{[\beta_{\parallel c}/(1 - \delta)]^{3/2}} \right. \\ &+ \left. \frac{\sqrt{2}(1 - \delta)}{[\beta_{\parallel c}/(1 - \delta) + \beta_{\parallel h}/\delta]^{3/2}} \right), \end{aligned} \quad (6g)$$

$$\bar{v}_{hh} = \frac{\sqrt{M} g \ln \Lambda'}{15} \left(\frac{\delta + \sqrt{2}}{[\beta_{\parallel h}/(1-\delta)]^{3/2}} + \frac{\sqrt{2}(1-\delta)}{[\beta_{\parallel c}/(1-\delta) + \beta_{\parallel h}/\delta]^{3/2}} \right), \quad (6h)$$

$$\bar{v}_{ch} = \frac{\sqrt{2M} g \ln \Lambda'}{3[\beta_{\parallel c}/(1-\delta) + \beta_{\parallel h}/\delta]^{3/2}}, \quad (6i)$$

$$\bar{v}_{pp} = \frac{g \ln \Lambda'}{15\beta_{\parallel p}^{3/2}}, \quad (6j)$$

$$\bar{v}_{cp} = \sqrt{\frac{2}{M}} \frac{g \ln \Lambda'}{3[\beta_{\parallel c}/(1-\delta)]^{3/2}}, \quad (6k)$$

$$\bar{v}_{hp} = \sqrt{\frac{2}{M}} \frac{g \ln \Lambda'}{3(\beta_{\parallel h}/\delta)^{3/2}}, \quad (6l)$$

$$\ln \Lambda' = \ln \left[\Lambda \left(\frac{1-\delta}{3} \frac{2\beta_{\perp c} + \beta_{\parallel c}}{\beta_{\text{ref}}} + \frac{\delta}{3} \frac{2\beta_{\perp h} + \beta_{\parallel h}}{\beta_{\text{ref}}} \right)^{3/2} \right]. \quad (6m)$$

Here, $\beta_{\text{ref}} = 8\pi n_{\text{[pcc]}} T_{\text{[eV]}}/B_{\text{[Gauss]}}^2$ denotes the reference beta value.

From the normalized Equations (6a)–(6m), it is seen that the dominant processes are electron collisions among core and halo components, as indicated by their normalized collision frequencies, $\bar{v}_{cc} \propto \mathcal{O}(\sqrt{M})$, $\bar{v}_{hh} \propto \mathcal{O}(\sqrt{M})$, and $\bar{v}_{ch} \propto \mathcal{O}(\sqrt{M})$. In contrast, the proton–proton collision frequency is of order unity, $\bar{v}_{pp} \propto \mathcal{O}(1)$, while the proton–electron collision frequency is even lower, of the order $\bar{v}_{cp} \sim \bar{v}_{hp} \propto \mathcal{O}(M^{-1/2})$. From this, we may simplify the problem by ignoring terms of order unity, $\mathcal{O}(1)$, and $\mathcal{O}(M^{-1/2})$. Here, we consider that the electron collision frequencies are of comparable order in that \bar{v}_{cc} , \bar{v}_{ch} , and \bar{v}_{hh} have a similar magnitude in an overall sense, although in detail, we expect a hierarchy of $\bar{v}_{cc} > \bar{v}_{ch} > \bar{v}_{hh}$. Nevertheless, when compared with \bar{v}_{pp} or \bar{v}_{cp} and \bar{v}_{hp} , these electron collision frequencies are much higher in the sense of the order-of-magnitude comparison. Thus, by retaining the dominant terms of order $\mathcal{O}(M^{1/2})$ only, we may ignore the proton dynamics, and we have a reduced set of dimensionless equations

$$\frac{d\beta_{\perp c}}{d\tau} = M^{\frac{1}{2}} [\mu_{cc}(\beta_{\parallel c} - \beta_{\perp c}) + \delta\mu_{hc}(\beta_{\perp h} - \beta_{\perp c})], \quad (7a)$$

$$\frac{d\beta_{\parallel c}}{d\tau} = 2M^{\frac{1}{2}} [\mu_{cc}(\beta_{\perp c} - \beta_{\parallel c}) + \delta\mu_{hc}(\beta_{\parallel h} - \beta_{\parallel c})], \quad (7b)$$

$$\frac{d\beta_{\perp h}}{d\tau} = M^{\frac{1}{2}} [\mu_{hh}(\beta_{\parallel h} - \beta_{\perp h}) + (1-\delta)\mu_{hc}(\beta_{\perp c} - \beta_{\perp h})], \quad (7c)$$

$$\frac{d\beta_{\parallel h}}{d\tau} = 2M^{\frac{1}{2}} [\mu_{hh}(\beta_{\perp h} - \beta_{\parallel h}) + (1-\delta)\mu_{hc}(\beta_{\parallel c} - \beta_{\parallel h})], \quad (7d)$$

where the relevant collisional relaxation frequencies are redefined by

$$\mu_{cc} = g' \left(\frac{1-\delta + \sqrt{2}}{[\beta_{\parallel c}/(1-\delta)]^{3/2}} + \frac{\sqrt{2}\delta}{[\beta_{\parallel c}/(1-\delta) + \beta_{\parallel h}/\delta]^{3/2}} \right), \quad (8a)$$

$$\mu_{hh} = g' \left(\frac{\delta + \sqrt{2}}{(\beta_{\parallel h}/\delta)^{3/2}} + \frac{\sqrt{2}(1-\delta)}{[\beta_{\parallel c}/(1-\delta) + \beta_{\parallel h}/\delta]^{3/2}} \right), \quad (8b)$$

$$\mu_{hc} = \frac{5\sqrt{2}g'}{[\beta_{\parallel c}/(1-\delta) + \beta_{\parallel h}/\delta]^{3/2}}, \quad (8c)$$

$$g' = \frac{g \ln \Lambda'}{15}. \quad (8d)$$

As with our previous paper, we take the typical 1 au value for the plasma density, $n \sim 8 \text{ cm}^{-3}$, the magnetic field intensity, $B \sim 5 \text{ nT} = 5 \times 10^{-5} \text{ Gauss}$, and the reference electron temperature, $T_e \sim 140,000 \text{ K} \sim 12 \text{ eV}$ (M. L. Stevens et al. 2018; K. G. Klein & D. Vech 2019). Given that 1 au equals $1.496 \times 10^8 \text{ km}$ and the typical solar wind speed is $\sim 300\text{--}600 \text{ km s}^{-1}$, the transit time for a typical solar parcel to traverse the distance the Sun–Earth separation is $\sim 2.5 \times 10^5\text{--}5 \times 10^5 \text{ s}$. We thus find that the normalized parameter g' is on the order $\mathcal{O}(10^{-7})$. We choose the maximum value for dimensionless time as 5×10^4 , following our previous paper (P. H. Yoon et al. 2024). In short, our choice of parameters is identical to those adopted in P. H. Yoon et al. (2024)

$$g' \sim 10^{-7}, \quad \tau_{\text{max}} \sim 5 \times 10^4. \quad (9)$$

Here, we note that we are working under a simplifying assumption that the protons are implicitly assumed to be isotropic and act as a neutralizing background. Recall that in our earlier work (P. H. Yoon et al. 2024), we have made an opposite assumption that the electrons are essentially isotropic and simply follow the ions in an adiabatic sense. Of course, both dynamics can be combined, but we are able to treat the proton and electron dynamics separately because of the fact that the very light electrons and protons move at a disparate timescale.

Following our previous study on the proton dynamics (P. H. Yoon et al. 2024), we consider a hypothetical ensemble of “initial” solar wind electron states. We consider an ensemble of core electrons and a separate ensemble of halo electrons. That is, we act as if the particles in these two populations are distinguishable. We assume that these initial ensemble states are associated with regions close to the coronal source and propagate to the near-Earth vicinity. However, as we stated in our previous paper, it should be emphasized that we are not attempting to model the realistic solar wind conditions close to the solar source (J. Huang et al. 2020; P. Mostafavi et al. 2024), but rather, our purpose is to cover a wide range of phase space uniformly by choosing a hypothetical ensemble of core and halo electrons at the initial time. In choosing the initial data

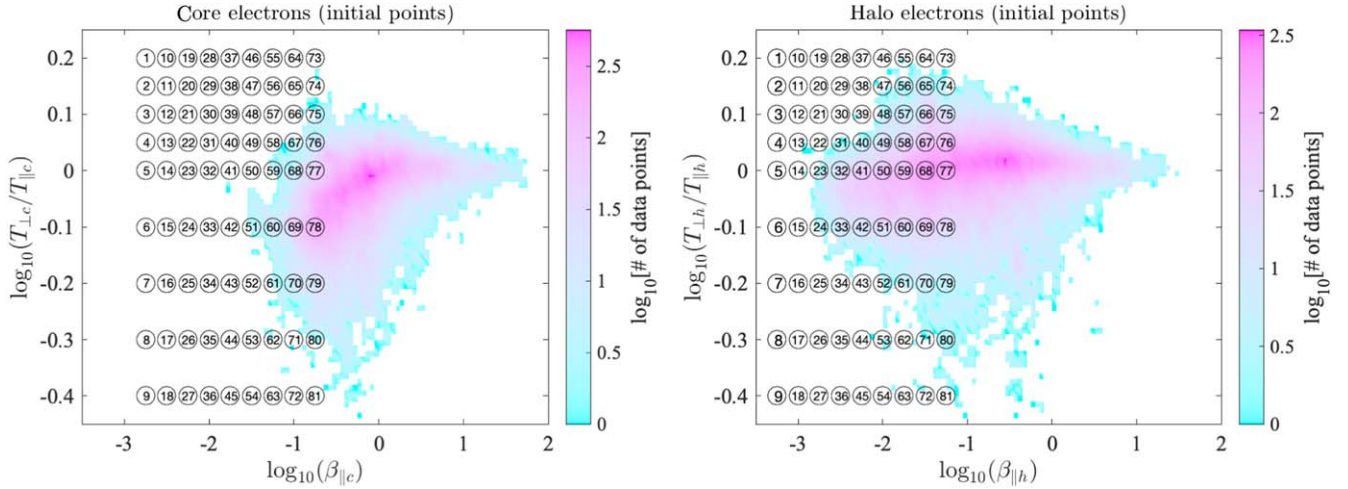


Figure 1. (Left) Initial ensemble positions of core electrons plotted against the backdrop of core electron data distribution. (Right) The same for the halo electrons, plotted against the backdrop of halo electron 2D distribution. The numerical designations signify the case numbers; 1–81. The colormap background data distributions use electron measurements from the Helios mission.

points for the dual core and halo electron populations, we need to be mindful that there are many possible combinations.

In Figure 1, the colormap of the occurrence distributions for the solar wind core and halo electrons is plotted as a backdrop. The left-hand panel plots the initial core electron ensemble points against the background of color-shaded core electron data distribution with the right-hand panel showing the same for the halo electrons. The color-shaded core and halo electron data distributions use electron measurements from the Helios mission, which consisted of two spacecraft (s/c) dedicated to making in situ observations of the inner heliosphere between 0.3 and 1 au. Helios 1 was launched on 1974 December 10, and Helios 2 on 1976 January 15, and both operated up to 1986. Helios 1 and 2 rank among the most important missions in Heliophysics, and the more than 11 yr of data returned by its spacecraft remain of paramount interest to researchers (E. Marsch 2012). Electrons with energy from 0.4 to 1658 eV were measured with a hemispherical electrostatic analyzer in one angular dimension and in 32 energy channels, part of the Helios Plasma Detectors Experiment E1 (R. Schwenn et al. 1975; H. Rosenbauer et al. 1977). Only 2D (in the ecliptic plane) electron distributions were provided (see, e.g., W. G. Pilipp et al. 1987a, for more details) at a time resolution of 40.5 s.

These measurements were analyzed to extract the properties of the three distinct solar wind electron populations, i.e., the thermal core, the suprathermal halo and the beam-like strahl (Š. Štverák et al. 2009, 2015; C. S. Salem et al. 2023), using least-square fit techniques. Since the measurements are only 2D, data preselection rules are required: (a) measurements for which the local interplanetary magnetic field is close to be perpendicular to the s/c spin axis (s/c spin axis being perpendicular to the ecliptic plane); (b) measurements for which the magnetic field vector is well aligned with the axis of one of the eight detector angular bins. The least-square fit technique applied to the selected sample of electron velocity distribution functions (VDFs) yield various moments of the core (c), halo (h), and strahl (s) populations, namely density N , velocity V , temperature parallel T_{\parallel} , and perpendicular T_{\perp} to the local magnetic field, as well as total heat flux Q (third-order moment of the VDFs). The condition (a) ensures that any temperature anisotropies with respect to the magnetic field are

accurately determined, and the condition (b) ensures that magnetic field aligned strahl is always well resolved by the detector.

Against the background of the data distribution, we display in Figure 1, one possible combination where the respective core and halo electron data points are arranged in a manner that has a similar repeating pattern for both species. That is, for case 1, we place both the core and halo electron initial states to occupy the upper-left corner points in their respective beta-anisotropy phase spaces, namely, $\beta_{\parallel c} = 10^{-2.75}$, $T_{\perp c}/T_{\parallel c} = 10^{0.2}$, and $\beta_{\parallel h} = 10^{-3.25}$, $T_{\perp h}/T_{\parallel h} = 10^{0.2}$, with case 2 for both core and halo chosen as the points immediately below those of case 1, that is, all the parameters are the same except that the temperature ratio is chosen slightly lower for both core and halo, $T_{\perp c}/T_{\parallel c} = 10^{0.15}$, $T_{\perp h}/T_{\parallel h} = 10^{0.15}$, so on and so forth, until we reach case 9. Then we repeat the pattern with a slightly higher value of parallel betas, $\beta_{\parallel c} = 10^{-2.5}$ and $\beta_{\parallel h} = 10^{-3}$, etc. Figure 1 shows this particular arrangement with each case indicated by the corresponding number. Of course, even with the initial states of core electrons as arranged in the left-hand panel of Figure 1, one could reshuffle the halo initial positions in any arbitrary arrays, and vice versa. Doing so could better span the phase space, but this leads to an additional complication, which arises for the multiple charged-particle populations and is distinct from our earlier study with the focus only on a single proton species. Note, however, that even though it is possible for one to choose a different set of initial conditions for these parameters, there is no observational incentive for it, especially for halo electrons. Halo parameters, as measured over a large span of radial distances (L. Berčič et al. 2000; M. Maksimovic et al. 2005; Š. Štverák et al. 2009; J. S. Halekas et al. 2020) are well within the assumed range. Consequently, in the present paper, we confine ourselves to the particular initial ensemble arrangement as shown in Figure 1.

We have solved the dynamical Equations (7a)–(7d), together with the dimensionless collision frequencies defined by Equations (8a)–(8d), under input parameters corresponding to the estimate given in Equation (9), namely, $g' = 10^{-7}$ and $\tau_{\max} = 5 \times 10^4$. These normalized input parameters are exactly identical to those adopted in our earlier study on the protons (P. H. Yoon et al. 2024). In the left-hand panel of Figure 2, the initial ensemble of core electron data points is

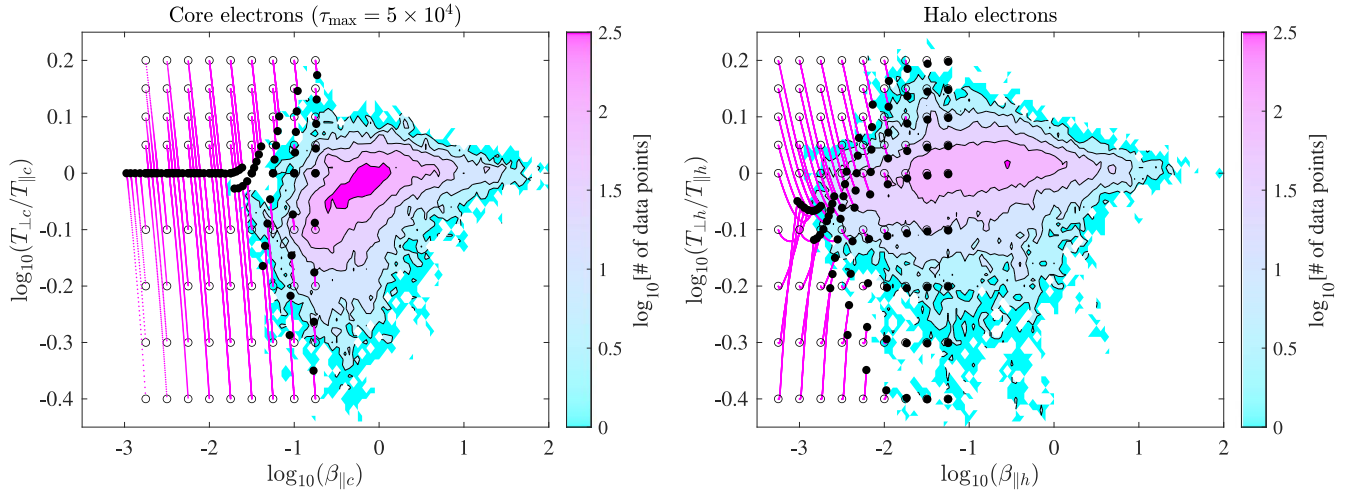


Figure 2. (Left) Initial ensemble of core electron data points are plotted with open circles; the dynamic paths in $(\beta_{\parallel c}, T_{\perp c}/T_{\parallel c})$ space are indicated with magenta curves; and the final states at $\tau_{\max} = \Omega_p t_{\max} = 5 \times 10^4$ are marked with black dots, against the background of core electron data distribution. (Right) The same for the halo electrons. An animation of this figure is available, where the ensemble trajectories from their initial positions, shown by open circles, are displayed for every time interval of $\Omega_p \Delta t = 10^3$, until the final computation period corresponding to $\Omega_p t = 5 \times 10^4$. The traces of the animated ensemble trajectories correspond to the magenta-colored curves in the inline figure. The real-time duration of the animation is 62 s.

(An animation of this figure is available in the [online article](#).)

plotted with open circles without the numerical designations. The ensemble of points are plotted in the background of core electron data distribution (2D histogram), as in Figure 1. The dynamic paths in $(\beta_{\parallel c}, T_{\perp c}/T_{\parallel c})$ space, as the core electrons relax via collisional processes, are indicated with magenta curves, and the final states at $\tau_{\max} = \Omega_p t_{\max} = 5 \times 10^4$ are marked with black dots. We have, of course, solved the halo electron equations concomitantly, and the results for the halo electrons are plotted in the right-hand panel of Figure 2, where we have followed the same procedure as we did for the core components. All of these theoretical results are plotted against the background of electron halo data distribution in 2D $(\beta_{\parallel h}, T_{\perp h}/T_{\parallel h})$ space. Judging from both panels in Figure 2, the “initial” ensemble points that are sufficiently far outside the boundary of the data distributions for both core and halo electrons are seen to swiftly move toward and settle around the outer perimeters on the low-beta sides of the respective data distributions. In contrast, those ensemble points that are already situated within the data distributions either barely move or move rather sluggishly. This finding is consistent with our earlier work on the protons in that, the collisional relaxation process is indeed a baseline explanation for the boundary of the charged-particle distributions on the low-beta side, as observed in the solar wind near 1 au. In the video file accompanying this paper, we also present the entire course of core and halo electron ensemble evolution, where the ensemble trajectories from their initial positions, shown by open circles, are displayed for every time interval of $\Omega_p \Delta t = 10^3$, until the final computation period corresponding to $\Omega_p t = 5 \times 10^4$. The traces of the animated ensemble trajectories correspond to the magenta-colored curves in the inline figure.

3. Regulation of Core–Halo Electron Temperature Anisotropies by Collective Instability Excitation

As for the boundaries associated with the 2D data distributions on the high-beta regime, it is known that the

temperature anisotropy-driven instabilities are largely responsible for their existence (P. H. Yoon 2017; D. Verscharen et al. 2022). Nevertheless, for the sake of completeness, we will demonstrate the effects of the temperature anisotropy instabilities and saturation by carrying out an ensemble of quasilinear relaxation calculations. We should note that the core and halo electron data boundaries on the high-beta side have received relatively less attention as compared to the similar high-beta boundary in the case of protons (Š. Štverák et al. 2008). For this purpose, we again consider an ensemble of initial core and halo electron ensemble points in the parameter space $(\beta_{\parallel}, T_{\perp}/T_{\parallel})$, but this time, corresponding to the high-beta regime, for both core and halo electrons. These initial ensemble points are meant to encompass the unstable regime. Among the temperature anisotropy instabilities of interest to us are the electromagnetic electron–cyclotron (EMEC) or whistler instability, in the case of excessive perpendicular temperature anisotropy, $T_{\perp} > T_{\parallel}$, and the electron firehose (EFH) instability in the case of excessive parallel temperature anisotropy, $T_{\parallel} > T_{\perp}$. For the sake of simplicity, we restrict ourselves to the parallel propagation of these unstable modes. This is certainly a simplification. It is known that oblique modes such as the electron mirror (P. Hellinger & v. Štverák 2018; M. Sarfraz et al. 2022) or oblique firehose (P. Hellinger & P. M. Trávníček 2008; R. A. López et al. 2022) modes act very rapidly on the electrons, so that this restriction might affect some of the early evolution in the ensemble calculation. One could certainly improve upon the present approach with a more sophisticated quasilinear simulation, but the purpose of the present study is to provide a baseline explanation. Such advanced computations could and should be the focus of a future endeavor. In any event, the evolution equation for the core and halo electron temperatures subject to these instabilities propagating in the parallel direction are discussed in standard references (e.g., M. Sarfraz et al. 2017; P. H. Yoon et al. 2017; S. M. Shaaban et al. 2019a, 2019b), and herewith we reproduce the quasilinear velocity moment equations derived

in these references

$$\frac{dT_{\perp c}}{dt} = -\frac{e^2}{2m_e c^2} \int \frac{dk}{k^2} \sum_{+,-} W_{\pm}(k) [(2A_c + 1)\gamma_k + \text{Im}(2i\gamma \pm \Omega_e)\eta_c^{\pm} Z(\zeta_c^{\pm})], \quad (10a)$$

$$\frac{dT_{\parallel c}}{dt} = \frac{e^2}{m_e c^2} \int \frac{dk}{k^2} \sum_{+,-} W_{\pm}(k) [(A_c + 1)\gamma_k + \text{Im}(\omega \pm \Omega_e)\eta_c^{\pm} Z(\zeta_c^{\pm})], \quad (10b)$$

$$\frac{dT_{\perp h}}{dt} = -\frac{e^2}{2m_e c^2} \int \frac{dk}{k^2} \sum_{+,-} W_{\pm}(k) [(2A_h + 1)\gamma_k + \text{Im}(2i\gamma \pm \Omega_e)\eta_h^{\pm} Z(\zeta_h^{\pm})], \quad (10c)$$

$$\frac{dT_{\parallel h}}{dt} = \frac{e^2}{m_e c^2} \int \frac{dk}{k^2} \sum_{+,-} W_{\pm}(k) [(A_h + 1)\gamma_k + \text{Im}(\omega \pm \Omega_e)\eta_h^{\pm} Z(\zeta_h^{\pm})], \quad (10d)$$

where $\omega = \omega_k + i\gamma_k$ denotes the complex conjugate solutions of the dispersion relation

$$0 = D(k, \omega) = c^2 k^2 - \sum_{a=c,h,p} \frac{\omega_{pa}^2}{\omega^2} [A_a + \eta_a^{\pm} Z(\zeta_a^{\pm})]. \quad (11)$$

In the above, the plus and minus signs signify the left-hand circularly polarized electron firehose (EFH) mode and the right-hand circularly polarized EMEC or whistler mode, respectively. The spectral magnetic field wave energy density corresponding to the left/right mode, $W_{\pm}(k) = \delta B_{\pm}^2(k)$, satisfies the wave kinetic equation

$$\partial W_{\pm}(k)/\partial t = 2\gamma_k W_{\pm}(k), \quad (12)$$

and various auxiliary quantities are defined by

$$A_a = \frac{T_{\perp a}}{T_{\parallel a}} - 1, \quad \zeta_a^{\pm} = \frac{\omega \pm \Omega_a}{k\alpha_{\parallel a}}, \quad \eta_a^{\pm} = \frac{(A_a + 1)\omega \pm A_a \Omega_a}{k\alpha_{\parallel a}}. \quad (13)$$

If we allow for negative real frequency, then both + and - signs can be discussed in a single framework by confining ourselves to only one sign associated with the plasma eigenmodes. For convenience, we choose to work with the lower sign. We may write the set of equations in terms of the same dimensionless quantities, which we have already introduced, namely, $\tau = \Omega_p t$, $\beta_{\perp, \parallel c, h} = 8\pi n_{c, h} T_{\perp, \parallel c, h} / B_0^2$, $\delta = n_h / n_0$, $A_{c, h} = T_{\perp c, h} / T_{\parallel c, h} - 1 = \beta_{\perp c, h} / \beta_{\parallel c, h} - 1$, as well as in terms of additional normalized variables

$$z = \frac{\omega_r}{\Omega_p}, \quad \gamma = \frac{\omega_i}{\Omega_p}, \quad \kappa = \frac{ck}{\omega_{pp}}, \quad M = \frac{m_p}{m_e}, \quad w(\kappa) d\kappa = \frac{\delta B^2(k)}{B_0^2} dk. \quad (14)$$

The result is

$$\frac{d\beta_{\perp c}}{d\tau} = -M(1 - \delta) \int \frac{d\kappa}{\kappa^2} w(\kappa) [(2A_c + 1)\gamma + \text{Im}(2i\gamma - M)\eta_c Z(\zeta_c)], \quad (15a)$$

$$\frac{d\beta_{\parallel c}}{d\tau} = 2M(1 - \delta) \int \frac{d\kappa}{\kappa^2} w(\kappa) [(A_c + 1)\gamma + \text{Im}(z - M)\eta_c Z(\zeta_c)], \quad (15b)$$

$$\frac{d\beta_{\perp h}}{d\tau} = -M\delta \int \frac{d\kappa}{\kappa^2} w(\kappa) [(2A_h + 1)\gamma + \text{Im}(2i\gamma - M)\eta_h Z(\zeta_h)], \quad (15c)$$

$$\frac{d\beta_{\parallel h}}{d\tau} = 2M\delta \int \frac{d\kappa}{\kappa^2} w(\kappa) [(A_h + 1)\gamma + \text{Im}(z - M)\eta_h Z(\zeta_h)], \quad (15d)$$

$$\zeta_c = \frac{(1 - \delta)^{1/2}(z - M)}{\kappa(M\beta_{\parallel c})^{1/2}}, \quad (15e)$$

$$\eta_c = \frac{(1 - \delta)^{1/2}[A_c(z - M) + z]}{\kappa(M\beta_{\parallel c})^{1/2}}, \quad (15f)$$

$$\zeta_h = \frac{\delta^{1/2}(z - M)}{\kappa(M\beta_{\parallel h})^{1/2}}, \quad (15g)$$

$$\eta_h = \frac{\delta^{1/2}[A_h(z - M) + z]}{\kappa(M\beta_{\parallel h})^{1/2}}. \quad (15h)$$

The wave intensities for each mode are computed by solving the wave kinetic equation, $\partial w(\kappa)/\partial \tau = 2\gamma w(\kappa)$. Here, we should point out that the ensemble calculation for the high-beta regime is carried out by ignoring the collisional relaxation altogether, and only the instability-induced relaxation processes are considered. It is possible to combine both effects, but the purpose of the present section is to isolate the effects of instabilities on the electron ensemble states in the high-beta regime. Note that we have made a similar delineation in our previous study of protons (P. H. Yoon et al. 2024), and herewith we follow the same practice so that a side-by-side comparison can be made.

In the numerical analysis, we find that the numerical complex root solving routine based upon the exact instantaneous dispersion relation (11) is quite cumbersome. Unlike the single proton species problem, which we considered in our previous paper (P. H. Yoon et al. 2024), the present situation of multiple electron species combined with the background protons renders the automatic complex root solving scheme at each time step along the quasilinear computation by numerical means somewhat unreliable. For this reason, we employ an approximation in which the collective relaxation by EMEC instability can be treated by a weak growth formalism, which assumes that the underlying nature of the wave-particle resonance is that of resonant variety. On the other hand, for the EFH instability, we find that the assumption of nonresonant instability is a reasonable first-cut approximation. The details can be found in Appendix B.

To investigate the temperature anisotropy relaxation by collective instability excitation we choose the initial data points for the dual core and halo electron populations in accordance with their operational range in the relatively high-beta regime.

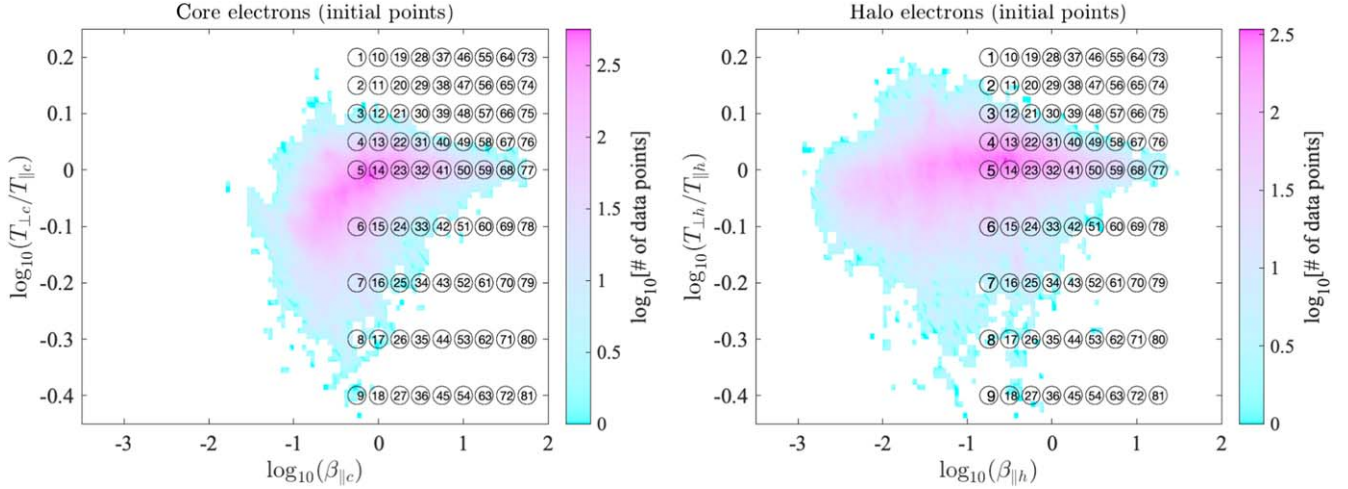


Figure 3. (Left) Initial ensemble positions in the case of collective instability saturation, for core electrons plotted against the backdrop of core electron data distribution. (Right) The same for the halo electrons, plotted against the backdrop of halo electron 2D distribution.

As with Figure 1, we choose one particular combination of initial ensemble points among many, where the core and halo electron data points are arranged in a manner that reflects a systematic repeating pattern. Specifically, for case 1, we place both the core and halo electron initial states to occupy the upper-left corner points in the high-beta regime corresponding to $\beta_{\parallel c} = 10^{-0.25}$, $T_{\perp c}/T_{\parallel c} = 10^{0.2}$, and $\beta_{\parallel h} = 10^{-0.75}$, $T_{\perp h}/T_{\parallel h} = 10^{0.2}$, followed by case 2, which is the same except for the temperature ratio, $T_{\perp c}/T_{\parallel c} = 10^{0.15}$, $T_{\perp h}/T_{\parallel h} = 10^{0.15}$, etc., until we reach case 9. We then repeat the pattern with a slightly higher value of parallel betas, namely, $\beta_{\parallel c} = 10^0$ and $\beta_{\parallel h} = 10^{-0.5}$, so on and so forth, in a systematic manner, until case 81. This pattern is analogous to Figure 1, except that these points occupy the high-beta regime. Figure 3 displays this particular arrangement with each case indicated by the corresponding case number. As with Figure 1, one could reshuffle the relative initial positions of core and halo electrons in any arbitrary arrays, but we will choose this specific initial ensemble arrangement for the sake of convenience.

We have solved the dynamical Equations (15a) and (15b), together with the wave kinetic equation. In solving for these equations one is faced with a vastly different timescale associated with the underlying instabilities. For EMEC instability (which operates for those initial ensemble points located in the region characterized by $T_{\perp} > T_{\parallel}$), the growth rate is on the order of electron-cyclotron frequency, while the EFH instability (which pertains to those ensemble points characterized by $T_{\parallel} > T_{\perp}$) growth rate is basically dictated by the proton cyclotron frequency—see Appendix B for examples of EMEC and EFH instability growth rates as well as the behavior associated with their real frequencies. Thus, one must choose a relatively short time step for the time integration of quasilinear equations that pertain to unstable EMEC mode. Specifically, we found that a normalized time step of $d\tau = 10^{-3}$ is required for a stable numerical integration. On the other hand, a substantially longer time step can be taken to be for the EFH case. It turns out that $d\tau = 10^{-2}$ is an optimal choice. Consequently, instead of solving the equations up to a fixed maximum normalized time τ_{\max} , we have instead made a different choice for $d\tau$ depending on whether the EMEC or EFH mode is unstable, and simply solved Equations (15a) and (15b) up to a fixed maximum number of iterations, that is,

$\#\text{iterations} = N_{\text{iteration}}$. Specifically, we have made an arbitrary choice of $N_{\text{iteration}} = 600$. The maximum computational time is, of course, determined by $\tau_{\max} = N_{\text{iteration}} d\tau$.

Figure 4 plots the result of numerical computation. As noted, in the case of EMEC instability, the quasilinear relaxation proceeds extremely fast (in the electron-cyclotron timescale), which required $d\tau = 10^{-3}$. Thus, the maximum number of iteration $N_{\text{iteration}} = 100$ translates to $\tau_{\max} = 0.6$, or $t_{\max} = 0.6\Omega_p^{-1}$. For EFH instability, on the other hand, for which the growth rate is much lower, we made the choice of $d\tau = 10^{-2}$, meaning that the maximum computational period in this situation is equivalent to $\tau_{\max} = 6$, or $t_{\max} = 6\Omega_p^{-1}$. In the left-hand panel of Figure 4, which shows the core electron dynamics, it is seen that the initial ensemble points for the core electrons have either all moved close to the marginally unstable states for EMEC or EFH instability, or, for those ensemble points that are below the marginal states, they remain unchanged. The final states are marked with black dots, while the intermediate dynamic paths are plotted with magenta-colored dotted lines.

The right-hand panel of Figure 4 plots the same result for the halo electrons. Again, it is seen that the initially EMEC unstable halo electron data points have moved close to the instability threshold curve. As for those halo electron ensemble points that are initially unstable to the (parallel) electron firehose (EFH) instability, we observe an interesting behavior that is somewhat different from that of the core electron. Instead of these points gradually moving close to the marginal stability threshold curve and settling down, they move past the marginal stability threshold curve and settle down in the vicinity defined by an isotropic condition, $\beta_{\perp h} \simeq \beta_{\parallel h}$. However, those halo electrons that are initially stable to the EFH instability excitation, that is, those electrons that are already located within the stability boundary, hardly move. Of course, the present instability-induced relaxation mechanism made a simplifying assumption of parallel propagation. In particular, obliquely propagating modes excited by the electron temperature anisotropy, namely, the electron mirror-mode (N. Noreen et al. 2017a; P. Hellinger & v. Štverák 2018; M. Sarfraz et al. 2022) and the oblique electron firehose mode (X. Li & S. R. Habbal 2000; E. Camporeale & D. Burgess 2008; P. Hellinger et al. 2014; M. E. Innocenti et al. 2019; R. A.

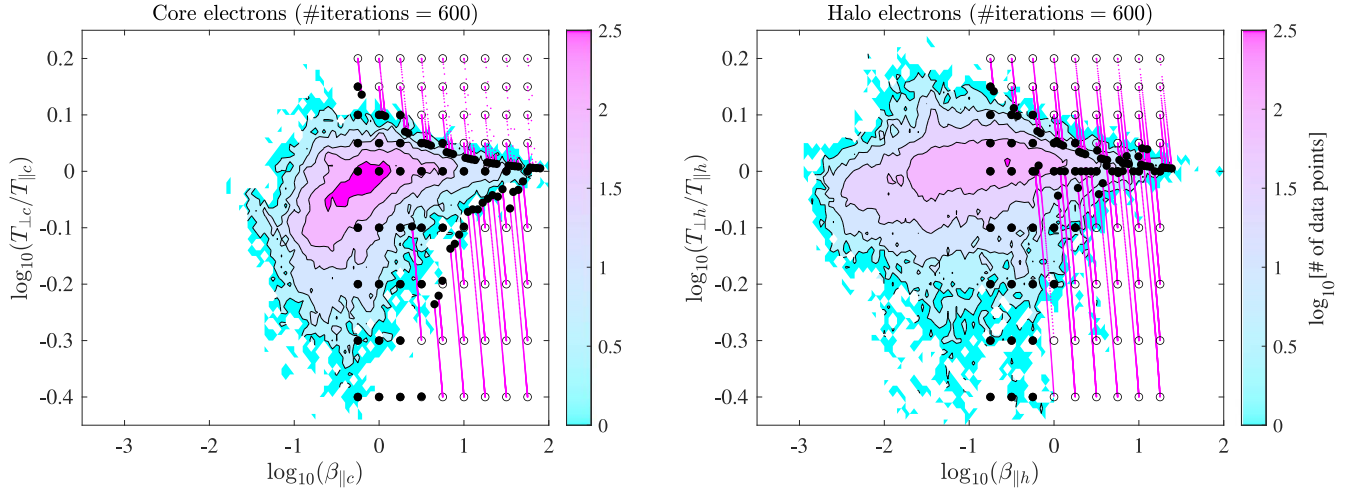


Figure 4. (Left) Initial ensemble of core electron data points in the case of collective relaxation is plotted with open circles; the dynamic paths in $(\beta_{\parallel c}, T_{\perp c}/T_{\parallel c})$ space are indicated with magenta curves; and the final states at $\tau_{\max} = \Omega_p t_{\max} = 10^2$ are marked with black dots, against the background of core electron data distribution. (Right) The same for the halo electrons. In the accompanying animation, the entire dynamics paths for the ensemble points that are subject to instability excitation and quasilinear relaxation, can be seen. Specifically, the ensemble trajectories from their initial positions are displayed for every 10 iteration interval, with the normalized time step in the case of EFH instability chosen as $dt = 10^{-2}\Omega_p^{-1}$, while for the EMEC instability, the same is chosen as $dt = 10^{-3}\Omega_p^{-1}$, until the final number of iterations corresponding to 600. The traces of the animated ensemble trajectories are the magenta-colored curves in the inline figure. The real-time duration of the animation is 62 s.

(An animation of this figure is available in the [online article](#).)

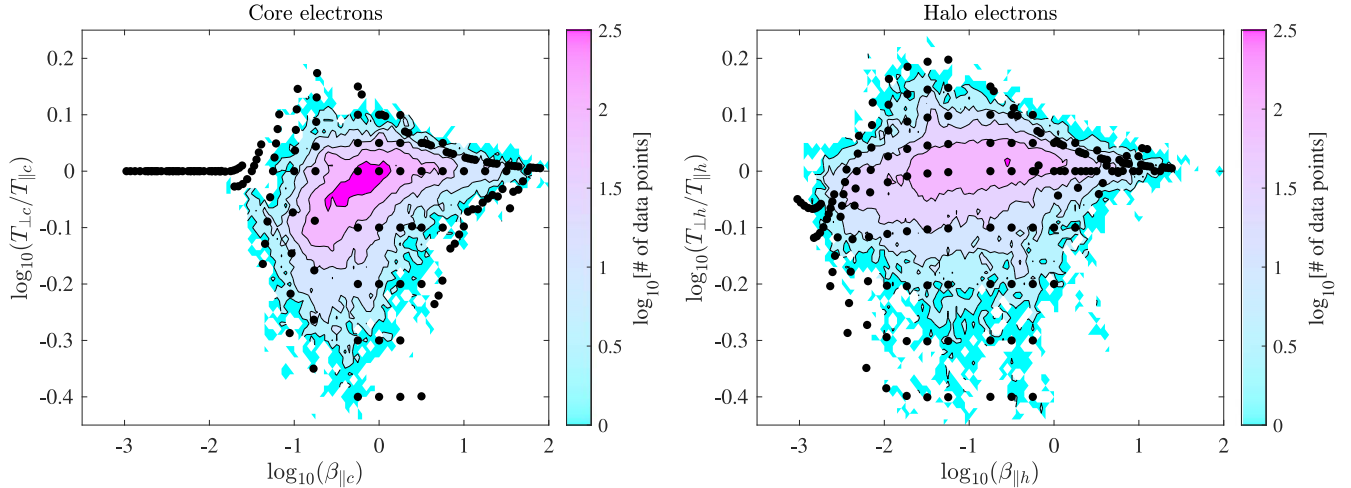


Figure 5. Combined results of combined dynamical ensemble calculation where the final states, plotted with black dots, are displayed against the backdrop of 2D solar wind electron frequency distribution. The final states are the same as those shown in Figures 2 and 4.

Lopez et al. 2019) may be important, which we ignored. However, these are also expected to be operative under conditions characterized by our choice of initial ensemble points. The impact of these unstable modes on the quasilinear dynamics is unknown at this point, and the subject is for future consideration. In spite of this, Figure 4 does provide a first-cut confirmation that the relaxation by parallel instability excitation and saturation is indeed important. As such, the instability-induced relaxation mechanism is an adequate explanation for the existence of the boundary associated with the solar wind electron data distribution on the high-beta regime, as observed in the near 1 au region of the heliosphere. This is, of course, to be expected to a certain extent, but the significance of the present work is that we have concretely demonstrated such a process. We also include a video that accompanies this article where the entire dynamics of ensemble evolution over the

iterations corresponding to $\#\text{iterations} = 10, 20, \dots, 600$, can be seen. Specifically, the ensemble trajectories from their initial positions are displayed for every 10 iteration interval, with the normalized time step in the case of EFH instability chosen as $dt = 10^{-2}\Omega_p^{-1}$, while for the EMEC instability, the same is chosen as $dt = 10^{-3}\Omega_p^{-1}$, until the final number of iterations corresponds to 600. The traces of the animated ensemble trajectories are the magenta-colored curves in the inline figure.

4. Summary

By way of summarizing our findings, we now combine the ensemble calculation results for both collisional relaxation and instability relaxation. The result is displayed in Figure 5, where we have plotted only the final states with dots, against the backdrop of the solar wind electron data distributions. To

reiterate, in the case of collisional relaxation, the computation is carried out up to $\Omega_p t = 5 \times 10^4$ —see Figure 2, while for the collective (instability-induced quasilinear) relaxation, we have iterated the computation up to the maximum number corresponding to $\#iterations = 600$, which corresponds to maximum computational time of $\Omega_p t = 0.6$ for EMEC instability and $\Omega_p t = 6$ for EFH instability—see Figure 4. This is done particularly for the sake of visualization of the accompanying animation file. If we adopt the maximum computational time instead, then those ensemble points corresponding to EMEC instability will evolve too quickly. Besides, once the fast-evolving EMEC instability reaches saturation, the ensemble points do not further evolve anyway, so adopting two different time steps does not affect the final outcome. The choice of the maximum number of iterations facilitates the visualization of the ensemble evolution. As is apparent, the final set of ensemble points largely overlap the actual core and halo electron data distributions. The present result complements the earlier work on the protons (P. H. Yoon et al. 2024).

In the present paper, we have paid attention to the temperature anisotropies associated with the core and halo electrons, but as we have noted previously, the core and halo electrons are frequently observed to possess a finite relative drift, as well as a net drift with respect to the background protons. For the sake of simplicity, we have not taken such features into account, but in the future, such properties should be taken into consideration. Of course, doing so will inevitably involve higher-dimensional representations of the electron (and proton) velocity distributions, involving relative drifts, betas, and temperature anisotropies. This will complicate the situation, but the present beta-anisotropy space is a first-cut useful construct that enables the physical interpretation of statistical volumes of spacecraft data. As such, the present paper, in and of itself, will not solve all of the problems associated with the expanding solar wind, but this work represents a useful summary on the issue of beta-temperature anisotropies for the solar wind electrons.

Another limitation relates to the fact that the halo electron population is ubiquitously characterized by nonthermal tail, which is often modeled with the bi-Kappa VDF. The present paper, on the other hand, modeled both the core and halo electrons by the bi-Maxwellian distributions. The impact of suprathermal bi-Kappa halo electrons must be investigated in the future. In this regard, some works have already addressed this issue as it relates to the regulation by instability excitation, see, e.g., M. Lazar et al. (2015). However, the collisional relaxation of bi-Kappa halo electrons in the present context, namely, the core and halo electron temperature relaxation problem, is yet to be addressed, although we should point out that some authors, including M. Maksimovic et al. (1997) and V. Pierrard et al. (1999), for instance, have already carried out the kinetic theory of collisional processes in the context of the exospheric model, and showed that the influence of Kappa populations leads to a decrease in collision frequency and an increase in the mean free path for the electrons.

Another caveat as it relates to the basic assumption in our paper is that we treat the electron core and halo as two distinguishable populations, although some studies imply that some of the “halo” electrons may migrate to “core” population and vice versa as the system evolves (V. Pierrard et al. 2022).

We do not include such a feature in our study, but it seems to be intuitively clear that this process, even if it is present at some point, cannot be abundant enough to significantly alter the electron VDFs, and this process is difficult to quantify. One possible approach to incorporating this feature is to consider the velocity moments of the entire electron VDF and compute the relaxation processes, but such an endeavor requires a new set of data analyses.

Another relevant issue is that we have ignored the “strahl” component altogether in our study. The observational data (e.g., Figure 1) do not differentiate between the slow and fast solar wind, but it is known that the strahl component is generally more prominent in the fast wind (W. G. Pilipp et al. 1987b, 1987; C. S. Salem et al. 2023). Moreover, some observations imply that the strahl electrons scatter into the halo population as the solar wind expands (Š. Štverák et al. 2009). The present work does not consider any of these higher-order aspects associated with the solar wind electrons, and thus, is limited in this sense as well.

We also remind the reader that our baseline model computation does not take into account other higher-order effects such as the radial expansion. Finally, in the present simplified approach, we have restricted ourselves to the instabilities propagating in directions parallel (and anti-parallel) to the ambient magnetic field. The influence of the obliquely propagating modes on the quasilinear dynamics is an important subject matter, which deserves a thorough consideration in the future.

Acknowledgments

This research was supported by NASA Award 80NSSC19K0827 (grant NNH18ZDA001N-HSR). This material is also based upon work funded by the Department of Energy (DE-SC0022963) through the NSF/DOE Partnership in Basic Plasma Science and Engineering. This research was also partially supported by NSF grant 2203321 to the University of Maryland. These results were also obtained (ML) in the framework of the projects WEAVE project—G.0025.23N / FI 706/31-1 (FWO-Vlaanderen/DFG-Germany) and SIDC Data Exploitation (ESA Prodex-12), and with support from the Ruhr-University Bochum and Katholieke Universiteit Leuven. J.S. was supported by basic research funding from the Korea Astronomy and Space Science Institute (KASI2024185002). The authors have no conflicts to disclose.

Data Availability

This paper deals with largely theoretical aspects except for the solar wind electron data that were used as the backdrop. The data used in this project were accessed through the SPFD CDA Web service cdaweb.gsfc.nasa.gov. The entire Helios data set is archived and maintained at the University of California Berkeley: <https://helios-data.ssl.berkeley.edu>. No new data are generated herewith.

Appendix A

Collisional Relaxation of the Anisotropic Temperatures

The formulation of core–halo electron collision problem starts from the same Balescu–Lenard–Guernsey kinetic equation, which we have employed in our previous paper (P. H. Yoon et al. 2024). The basic form of the collisional

kinetic equation is given by

$$\begin{aligned} \frac{\partial f_a(\mathbf{v})}{\partial t} &= -\frac{e_a^2}{m_a^2} \int d\mathbf{k} \int d\omega \frac{\mathbf{k}}{k} \cdot \frac{\partial}{\partial \mathbf{v}} \text{Im} \frac{1}{\omega - \mathbf{k} \cdot \mathbf{v} + i0} \\ &\quad \times \left(\frac{m_a \text{Im} \epsilon(\mathbf{k}, \omega)}{2\pi^3 k |\epsilon(\mathbf{k}, \omega)|^2} f_a(\mathbf{v}) + E_{\mathbf{k}, \omega}^2 \frac{\mathbf{k}}{k} \cdot \frac{\partial f_a(\mathbf{v})}{\partial \mathbf{v}} \right), \\ E_{\mathbf{k}, \omega}^2 &= -\sum_a \frac{2e_a^2}{\pi^2 k^2 |\epsilon(\mathbf{k}, \omega)|^2} \int d\mathbf{v} \text{Im} \frac{f_a(\mathbf{v})}{\omega - \mathbf{k} \cdot \mathbf{v} + i0}, \\ \epsilon(\mathbf{k}, \omega) &= 1 + \sum_a \frac{4\pi e_a^2}{m_a k^2} \int d\mathbf{v} \frac{\mathbf{k} \cdot \partial f_a(\mathbf{v}) / \partial \mathbf{v}}{\omega - \mathbf{k} \cdot \mathbf{v} + i0}. \end{aligned} \quad (\text{A1})$$

Note that if we replace the dielectric constant by unity ($\epsilon \rightarrow 1$), then we have the Landau collision integral, which formed the basis of earlier works (V. I. Kogan 1961; P. Hellinger & P. M. Travnicek 2009, 2010; W. Jubeh & I. A. Barghouthi 2017). Here, $f_a(\mathbf{v})$ is the VDF (with the normalization, $\int d\mathbf{v} f_a(\mathbf{v}) = n_a$, where n_a is the ambient density); e_a and m_a stand for the electric charge and mass for charged-particle species labeled a ; $E_{\mathbf{k}, \omega}^2$ is the square of the steady-state electric field spectral amplitude; and $\epsilon(\mathbf{k}, \omega)$ denotes the dielectric constant. From here, we take the same procedure as in our previous paper, namely, we take the velocity moments of the collisional kinetic Equation A1, $n_a T_{\perp a} = \int d\mathbf{v} m_a (v_{\perp}^2/2) f_a(\mathbf{v})$ and $n_a T_{\parallel a} = \int d\mathbf{v} m_a v_{\parallel}^2 f_a(\mathbf{v})$, where the \perp and \parallel denote directions with respect to the direction of the ambient magnetic field, which is implicitly assumed, and $T_{\perp a}$ and $T_{\parallel a}$ represent the perpendicular and parallel kinetic temperatures. Under the assumption of bi-Maxwellian VDF, $f_a(\mathbf{v}) = n_a \pi^{-3/2} \alpha_{\perp a}^{-2} \alpha_{\parallel a}^{-1} \exp(-v_{\perp}^2/\alpha_{\perp a}^2 - v_{\parallel}^2/\alpha_{\parallel a}^2)$, where $\alpha_{\perp a} = (2T_{\perp a}/m_a)^{1/2}$ and $\alpha_{\parallel a} = (2T_{\parallel a}/m_a)^{1/2}$ signify the perpendicular and parallel thermal speeds, respectively, we may derive the governing dynamical equations that describe the evolution of $T_{\perp a}$ and $T_{\parallel a}$. The detailed steps are already outlined in our previous paper, and the result is given by

$$\begin{aligned} \frac{dT_{\perp a}}{dt} &= \frac{\pi^{1/2} e_a^2}{m_a} \int d\mathbf{k} \frac{k_{\perp}^2}{k^2} \int \frac{d\omega}{\omega} \left[-\frac{\text{Im} \epsilon(\mathbf{k}, \omega)}{\pi^3 |\epsilon(\mathbf{k}, \omega)|^2} \frac{\zeta_a^2 T_{\perp a}}{\omega} \right. \\ &\quad \left. + E_{\mathbf{k}, \omega}^2 \left(1 - \frac{k^2 \alpha_{\perp a}^2 \zeta_a^2 (1 - 2\zeta_a^2)}{(\omega - k_{\parallel} V_a)^2} \right) \right] \zeta_a e^{-\zeta_a^2}, \\ \frac{dT_{\parallel a}}{dt} &= \frac{2\pi^{1/2} e_a^2}{m_a} \int d\mathbf{k} \frac{k_{\parallel}^2}{k^2} \int \frac{d\omega}{\omega} \left[-\frac{\text{Im} \epsilon(\mathbf{k}, \omega)}{\pi^3 |\epsilon(\mathbf{k}, \omega)|^2} \frac{\zeta_a^2 T_{\parallel a}}{\omega} \right. \\ &\quad \left. + E_{\mathbf{k}, \omega}^2 \left(1 - \frac{k^2 \alpha_{\parallel a}^2 \zeta_a^2 (1 - 2\zeta_a^2)}{(\omega - k_{\parallel} V_a)^2} \right) \right] \zeta_a e^{-\zeta_a^2}, \\ \zeta_a &= \frac{\omega}{(k_{\perp}^2 \alpha_{\perp a}^2 + k_{\parallel}^2 \alpha_{\parallel a}^2)^{1/2}}, \end{aligned} \quad (\text{A2})$$

together with the expressions for the steady-state wave spectrum, $E_{\mathbf{k}, \omega}^2$, and the dielectric constant, $\epsilon(\mathbf{k}, \omega)$

$$\begin{aligned} E_{\mathbf{k}, \omega}^2 &= \sum_b \frac{2n_b e_b^2}{\pi^{3/2} k^2 |\epsilon(\mathbf{k}, \omega)|^2} \frac{\zeta_b e^{-\zeta_b^2}}{\omega}, \\ \epsilon(\mathbf{k}, \omega) &= 1 + \sum_b \frac{8\pi n_b e_b^2}{m_b} \frac{\zeta_b^2 [1 + \zeta_b Z(\zeta_b)]}{\omega^2}, \end{aligned} \quad (\text{A3})$$

where ζ_b is defined exactly as in Equation (A2), except for the label b , and $Z(z) = \pi^{-1/2} \int_{-\infty}^{\infty} dt e^{-t^2} (t-z)^{-1}$, $\text{Im}(z) > 0$ represents the plasma dispersion (or Fried–Conte) function. Up to this point, the results are identical to that already discussed in our previous paper, where we also discuss that upon approximating the dielectric constant via $1/|\epsilon(\mathbf{k}, \omega)|^2 \approx |1 + 1/k^2 \lambda_D^2|^{-2}$, and subsequently approximating the integration over the modulus of the wavevector by $\int_0^{\infty} dk k^3 \lambda_D^4 (1 + k^2 \lambda_D^2)^{-2} \rightarrow \int_0^{4\pi n \lambda_D^3} dk k^3 \lambda_D^4 (1 + k^2 \lambda_D^2)^{-2} \approx \ln \Lambda$, where $\lambda_D^2 = T_e / (4\pi n e^2)$ is the square of the Debye length, $T_e = (T_{\perp e} + 2T_{\parallel e})/3$ being the electron temperature, and $\Lambda = 4\pi n \lambda_D^3$, then the remaining ω integral and the integration over the wavevector polar angle can be carried out exactly. This was true, particularly for the case of proton–proton collisions. However, for a general situation that involves like-particle collisions as well as collisions among different charged-particle species, the general result is rather cumbersome, and the final result customarily involves mathematical representation in terms of the generalized hypergeometric functions. The purpose of the present analysis is to derive sufficiently accurate and useful forms of various collision frequencies without going through laborious mathematical manipulations.

For this purpose, it is instructive to define a quantity

$$\eta_a = \frac{1}{(k_{\perp}^2 \alpha_{\perp a}^2 + k_{\parallel}^2 \alpha_{\parallel a}^2)^{1/2}}. \quad (\text{A4})$$

Making use of Equations (A2) and (A3) under the approximation of $1/|\epsilon(\mathbf{k}, \omega)|^2 \approx |1 + 1/k^2 \lambda_D^2|^{-2}$, it is possible to recast Equations (A2) and (A3) in the following form:

$$\begin{aligned} \frac{dT_{\perp a}}{dt} &= \sum_b \frac{2n_b e_b^2}{\pi^{1/2} m_a} \int d\mathbf{k} \frac{k_{\perp}^2 k^2 \lambda_D^4}{|1 + k^2 \lambda_D^2|^2} \frac{\eta_a^3 \eta_b^3}{(\eta_a^2 + \eta_b^2)^{3/2}} \\ &\quad \times \left(\frac{1}{k^2} \frac{\eta_a^2 + \eta_b^2}{\eta_a^2 \eta_b^2} - \frac{2T_{\perp a}}{m_a} \frac{m_a + m_b}{m_b} \right), \\ \frac{dT_{\parallel a}}{dt} &= \sum_b \frac{4n_b e_b^2}{\pi^{1/2} m_a} \int d\mathbf{k} \frac{k_{\parallel}^2 k^2 \lambda_D^4}{|1 + k^2 \lambda_D^2|^2} \frac{\eta_a^3 \eta_b^3}{(\eta_a^2 + \eta_b^2)^{3/2}} \\ &\quad \times \left(\frac{1}{k^2} \frac{\eta_a^2 + \eta_b^2}{\eta_a^2 \eta_b^2} - \frac{2T_{\parallel a}}{m_a} \frac{m_a + m_b}{m_b} \right), \end{aligned} \quad (\text{A5})$$

where we have carried out the ω integration. Aside from the approximation for $\epsilon(\mathbf{k}, \omega)$, this result is exact. At this stage of the formalism, it is appropriate to introduce a useful

approximation, that is, we simplify the following object of interest:

$$\frac{\eta_a^3 \eta_b^3}{(\eta_a^2 + \eta_b^2)^{3/2}} \approx \frac{1}{k^3 (\alpha_{\parallel a}^2 + \alpha_{\parallel b}^2)^{3/2}}, \quad (\text{A6})$$

and carry out the angular integration within $\int dk = 2\pi \int_0^\infty dk k^2 \int_{-1}^1 d(\cos \theta)$, that is, the θ integration. The remaining k integral with an appropriate upper limit cutoff leads to the so-called Coulomb logarithm, as already explained. The resulting approximate form of the collisional temperature relaxation equation is as shown below,

$$\begin{aligned} \frac{dT_{\perp a}}{dt} &= \sum_b \frac{8\sqrt{2}\pi^{1/2}n_b e_a^2 e_b^2 \ln \Lambda}{15m_a(T_{\parallel a}/m_a + T_{\parallel b}/m_b)^{3/2}} \\ &\quad \times \left(\frac{T_{\parallel a}}{m_a} - \frac{T_{\perp a}}{m_a} + \frac{4T_{\perp b}}{m_b} - \frac{5T_{\perp a}}{m_b} + \frac{T_{\parallel b}}{m_b} \right), \\ \frac{dT_{\parallel a}}{dt} &= \sum_b \frac{16\sqrt{2}\pi^{1/2}n_b e_a^2 e_b^2 \ln \Lambda}{15m_a(T_{\parallel a}/m_a + T_{\parallel b}/m_b)^{3/2}} \\ &\quad \times \left(\frac{T_{\perp a}}{m_a} - \frac{T_{\parallel a}}{m_a} + \frac{T_{\perp b}}{m_b} + \frac{3T_{\parallel b}}{2m_b} - \frac{5T_{\parallel a}}{2m_b} \right), \quad (\text{A7}) \end{aligned}$$

and we find that this set of equations provides a convenient platform for calculating various collisional relaxation frequencies for plasmas that comprise multiple charged-particle species. One can easily verify that Equation (A7) reduces to the correct proton–proton collisional temperature relaxation equation derived in our previous paper. As the purpose of the present paper is to discuss the collisional relaxation of solar wind electrons, which are customarily treated as being made of the core and halo components, we subsequently restrict our analysis to such a problem. The dominant core (c) population is made of denser, colder electrons, while the tenuous halo (h) electron component is described by a much higher temperature. Applying the density conservation $n_p = n = n_c + n_h$ and explicitly writing out the equations for each species (protons, p , core and halo electrons, c and h), we arrive at the set of equations introduced in the main body of the text, that is, Equations (1a)–(2f).

Appendix B Approximate Analysis of Dispersion Relation

In the quasilinear theory of electromagnetic electron–cyclotron (EMEC) and (parallel) electron firehose (EFH) instabilities it is necessary to solve the instantaneous dispersion relation (11) at each time during the numerical integration of the velocity moment Equations (15a)–(15c). The dimensionless form of (11) is given by

$$\begin{aligned} 0 &= \kappa^2 + \xi_p Z(\zeta_p) - M(1 - \delta)[A_c + \eta_c Z(\eta_c)] \\ &\quad - M\delta[A_h + \eta_h Z(\zeta_h)], \\ \xi_p &= \frac{z}{\kappa\beta_p^{1/2}}, \quad \zeta_p = \frac{z + 1}{\kappa\beta_p^{1/2}}, \quad (\text{B1}) \end{aligned}$$

where $\beta_p = 8\pi n T_p / B_0^2$ is the proton beta, and other quantities, namely, ζ_c , η_c , ζ_h , and η_h are defined in Equation (15c). The EMEC instability operates on a timescale of the inverse

electron gyro period, while the EFH mode timescale is defined by the proton cyclotron period. As a result of these vastly different instability timescales, the numerical integration of velocity moment Equations (15a) and (15b) becomes time consuming. To simplify the numerical efforts we have devised an efficient approximate analytical method to determine the instantaneous roots. For the EMEC mode, we find that the resonant wave-particle approximation combined with the weak growth rate formalism is applicable. Under such a scheme, the real frequency of the EMEC mode is determined by approximating the Z function by its asymptotic form, $Z(\zeta) \approx -\zeta^{-1} + i\pi^{1/2}e^{-\zeta^2}$, and by retaining only the real part thereof. The growth rate is determined by the textbook approach of balancing the imaginary part of Equation (B1) under the Z function expansion, combined with the Taylor series expansion of the remaining term, the so-called Landau formalism. The resulting real frequency and the growth rate for the EMEC instability is given in normalized form by

$$\begin{aligned} z &= \frac{\kappa^2(M - 1) + |\kappa|(M + 1)^{1/2}[\kappa^2(M + 1) + 4M]^{1/2}}{2(M + 1 + \kappa^2)}, \\ \gamma &= \frac{\pi^{1/2}(G_p + G_c + G_h)}{2(M + 1 + \kappa^2)z - \kappa^2(M - 1)}, \quad (\text{B2}) \end{aligned}$$

where $z = \omega_r / \Omega_p$, $\gamma = \omega_i / \Omega_p$, $\kappa = ck / \omega_{pp}$, and $M = m_p / m_e$ are already introduced in Equation (14), and G_p , G_c , and G_h represent the contribution to the wave growth/damping rate from the protons and core and halo electrons, respectively

$$\begin{aligned} G_p &= z(z - M)\zeta_p e^{-\zeta_p^2}, \\ G_c &= M(1 - \delta)(z + 1)(A_c z + z - MA_c)\zeta_c e^{-\zeta_c^2}, \\ G_h &= M\delta(z + 1)(A_h z + z - MA_h)\zeta_h e^{-\zeta_h^2}, \quad (\text{B3}) \end{aligned}$$

with ζ_p being defined in Equation (B1), and ζ_c and ζ_h being defined in Equation (15c). We found that this form of wave dispersion relation and growth rate quite accurately approximates the actual numerical roots corresponding to the unstable EMEC mode, provided the maximum growth rate is slightly adjusted by a multiplicative scale factor, that is, by adjusting the analytical growth rate, $\gamma \rightarrow f_{\text{scale}}\gamma$. Note that a similar procedure was first introduced in a recent pair of papers (R. A. López et al. 2023; P. H. Yoon et al. 2023), where by adjusting the analytical growth rate with an empirical scaling factor, an excellent agreement between the fully numerical complex roots and analytical formulae are obtained for the proton cyclotron and mirror-mode instabilities. Moreover, a similarly excellent agreement was achieved between the quasilinear theory with the scaling factor and the hybrid particle-in-cell code simulation.

As for the EFH mode, we found that the nonresonant instability approximation is applicable. In this approach, the Z function is approximated by its asymptotic form, but the expansion is kept up to the second order while ignoring the imaginary part, $Z(\zeta) \approx -1/\zeta - 1/(2\zeta^3)$. This is done for the core and halo linear responses. For the isotropic protons, only the leading order expansion is necessary. After inserting these

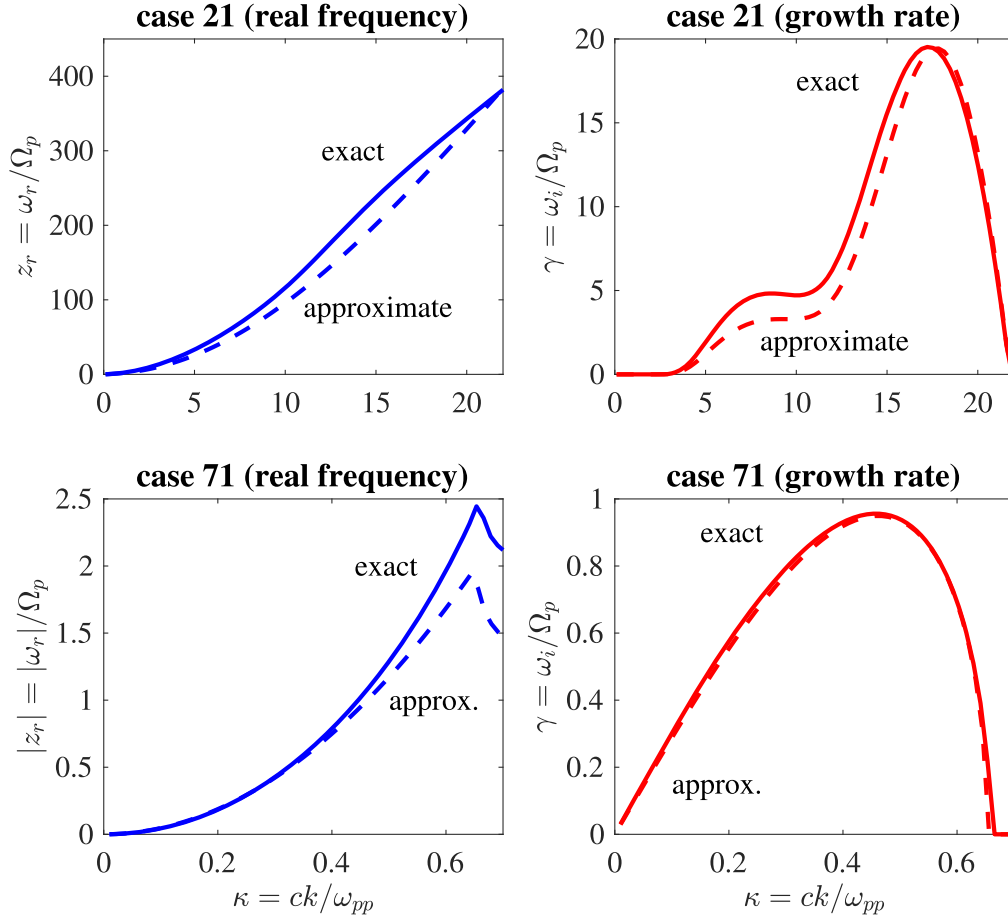


Figure 6. Examples of exact vs. approximate dispersion relations. (Top) Real frequency and growth rate for EMEC instability (case 21). Solid curves are exact numerical solutions based upon Equation (B1), while the dashed curves are approximate solutions, Equation (B2), except that γ is multiplied with $f_{\text{scale}} = 0.625$. (Bottom) Real frequency and growth rate for EFH instability (case 71). Solid curves are exact numerical solutions based upon Equation (B1), while the dashed curves are approximate solutions based on Equation (B4), except that γ is multiplied with $f_{\text{scale}} = 0.95$.

Table 1
List of Empirical Scale Factor f_{scale} for Adjusting the Maximum Growth Rate

| f_{scale} | | | | | | | | | |
|-----------------------|-------------------------|-------------------------|-------------------------|-------------------------|------------------------|-------------------------|-------------------------|-------------------------|--|
| (1) 0.64 ^C | (10) 0.6 ^C | (19) 0.64 ^C | (28) 0.64 ^C | (37) 0.69 ^C | (46) 0.78 ^C | (55) 0.925 ^C | (64) 1.13 ^C | (73) 1.41 ^C | |
| (2) 0.69 ^C | (11) 0.625 ^C | (20) 0.61 ^C | (29) 0.61 ^C | (38) 0.65 ^C | (47) 0.73 ^C | (56) 0.86 ^C | (65) 1.03 ^C | (74) 1.28 ^C | |
| (3) 0.93 ^C | (12) 0.7 ^C | (21) 0.625 ^C | (30) 0.6 ^C | (39) 0.61 ^C | (48) 0.67 ^C | (57) 0.765 ^C | (66) 0.915 ^C | (75) 1.12 ^C | |
| (4) 0.95 ^C | (13) 0.94 ^C | (22) 0.92 ^C | (31) 0.655 ^C | (40) 0.595 ^C | (49) 0.59 ^C | (58) 0.64 ^C | (67) 0.73 ^C | (76) 0.88 ^C | |
| (5) S | (14) S | (23) S | (32) S | (41) S | (50) S | (59) S | (68) S | (77) S | |
| (6) S | (15) S | (24) S | (33) S | (42) S | (51) 0.55 ^F | (60) 0.8 ^F | (69) 0.88 ^F | (78) 0.92 ^F | |
| (7) S | (16) S | (25) S | (34) S | (43) 0.65 ^F | (52) 0.85 ^F | (61) 0.9 ^F | (70) 0.94 ^F | (79) 0.96 ^F | |
| (8) S | (17) S | (26) S | (35) 0.35 ^F | (44) 0.81 ^F | (53) 0.88 ^F | (62) 0.925 ^F | (71) 0.95 ^F | (80) 0.97 ^F | |
| (9) S | (18) S | (27) S | (36) 0.65 ^F | (45) 0.85 ^F | (54) 0.9 ^F | (63) 0.935 ^F | (72) 0.96 ^F | (81) 0.965 ^F | |

Note. Numbers within the bracket correspond to positions of initial ensemble points as indicated by Figure 1. Those cases that are stable are indicated by S. Ensemble points unstable to EMEC or EFH instability are denoted by superscript C or F, respectively.

approximate forms of relevant Z functions, we then retain the resonant denominators of order $(z - M)^{-1}$, which leads to






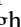
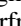


$$\begin{aligned}
 0 &= (M + 1 + \kappa^2)z^2 - \kappa^2(M - 1)z \\
 &\quad - M\kappa^2 + \frac{M^2\kappa^2(\beta_{\perp} - \beta_{\parallel})(z + 1)}{2(z - M)}, \\
 \beta_{\perp} &= \beta_{\perp c} + \beta_{\perp h}, \quad \beta_{\parallel} = \beta_{\parallel c} + \beta_{\parallel h}.
 \end{aligned} \tag{B4}$$

Among the complex roots of this cubic equation, the solution corresponding to the positive imaginary part represents the unstable EFH mode. As with the resonant EMEC instability, however, we also found that it is necessary to adjust the maximum growth rate of the unstable root by an appropriate scaling factor, $\gamma \rightarrow f_{\text{scale}}\gamma$. By trial and error, we have compiled the list of scale factors, f_{scale} , for each case, and displayed the result in Table 1. The number enclosed by the bracket is the

initial ensemble point as indicated by Figure 1. Of all the cases, those corresponding to stable initial states are indicated by S. Those initial states that are unstable to either EMEC or EFH instability excitation are indicated by the superscript *C* or *F*.

To illustrate the present scheme, we plot in Figure 6, the comparison between the exact and approximate dispersion relations for cases 21 and 71, which are chosen randomly. For both cases, the analytical growth rates are adjusted with the respective scale factor listed in Table 1. As is apparent, the comparisons are quite reasonable. Other cases also show good agreements. It is also apparent that while the EMEC mode is controlled by the electron dynamics (with high normalized wave frequency and growth rate), the EFH mode is essentially a proton mode with both the real frequency and growth rate lying in the vicinity of the proton gyrofrequency.

ORCID iDs

Peter H. Yoon  <https://orcid.org/0000-0001-8134-3790>
 Chadi S. Salem  <https://orcid.org/0000-0002-6536-1531>
 Kristopher G. Klein  <https://orcid.org/0000-0001-6038-1923>
 Mihailo M. Martinović  <https://orcid.org/0000-0002-7365-0472>
 Rodrigo A. López  <https://orcid.org/0000-0003-3223-1498>
 Jungjoon Seough  <https://orcid.org/0000-0002-1723-5944>
 Muhammad Sarfraz  <https://orcid.org/0000-0002-3082-6458>
 Marian Lazar  <https://orcid.org/0000-0002-8508-5466>
 Shaaban M. Shaaban  <https://orcid.org/0000-0003-0465-598X>

References

- Adrian, M. L., Vinas, A. F., Moya, P. S., & Wendel, D. E. 2016, *ApJ*, **833**, 49
 Bale, S. D., Drake, J. F., McManus, M. D., et al. 2023, *Natur*, **618**, 252
 Bale, S. D., Kasper, J. C., Howes, G. G., et al. 2009, *PhRvL*, **103**, 211101
 Berčič, L., Larson, D., Whittlesey, P., et al. 2000, *ApJ*, **528**, 88
 Camporeale, E., & Burgess, D. 2008, *JGRA*, **113**, A07107
 Chen, C. H. K., Matteini, L., Schekochihin, A. A., Stevens, M. L., et al. 2016, *ApJL*, **825**, L26
 Chitta, L. P., Zhukov, A. N., Berghmans, D., et al. 2023, *Sci*, **381**, 867
 Feldman, W. C., Asbridge, J. R., Bame, S. J., Montgomery, M. D., & Gary, S. P. 1975, *JGR*, **80**, 4181
 Fox, N. J., Velli, M. C., Bale, S. D., et al. 2016, *SSRv*, **204**, 7
 Gary, S. P., Skoug, R. M., Steinberg, J. T., & Smith, C. W. 2001, *GeoRL*, **28**, 2759
 Gary, S. P., Wang, J., Winske, D., & Fuselier, S. A. 1997, *JGR*, **102**, 27159
 Halekas, J. S., Whittlesey, P., Larson, D. E., et al. 2020, *ApJS*, **246**, 22
 He, J., Tu, C., March, E., Bourouaine, S., & Pei, Z. 2013, *ApJ*, **773**, 72
 Hellinger, P., & Trávníček, P. M. 2008, *JGRA*, **113**, A10109
 Hellinger, P., & Trávníček, P. M. 2009, *PhPI*, **16**, 054501
 Hellinger, P., & Trávníček, P. M. 2010, *JCoPh*, **229**, 5432
 Hellinger, P., & Trávníček, P. M. 2014, *ApJL*, **784**, L15
 Hellinger, P., Trávníček, P. M., Decyk, V. K., & Schriver, D. 2014, *JGRA*, **119**, 59
 Hellinger, P., Trávníček, P., Kasper, J. C., & Lazarus, A. J. 2006, *GeoRL*, **33**, L09101
 Hellinger, P., & Štverák, V. 2018, *JPIPh*, **84**, 905840402
 Huang, J., Kasper, J. C., Vech, D., et al. 2020, *ApJS*, **246**, 70
 Innocenti, M. E., Tenerani, A., Boella, E., & Velli, M. 2019, *ApJ*, **883**, 146
 Jube, W., & Barghouti, I. A. 2017, *PhPI*, **24**, 122104
 Kasper, J. C., Klein, K. G., Weber, T., et al. 2017, *ApJ*, **849**, 126
 Kasper, J. C., Lazarus, A. J., & Gary, S. P. 2002, *GeoRL*, **29**, 1839
 Kasper, J. C., Lazarus, A. J., Gary, S. P., & Szabo, A. 2003, in *AIP Conf. Ser.*, *Solar Wind Ten*, 679, ed. M. Velli et al. (Melville, NY: AIP), 538
 Klein, K. G., Alterman, B. L., Stevens, M. L., Vech, D., & Kasper, J. C. 2018, *PhRvL*, **120**, 205102
 Klein, K. G., Martinović, M., Standsby, D., & Horbury, T. S. 2019, *ApJ*, **887**, 234
 Klein, K. G., & Vech, D. 2019, *RNAAS*, **3**, 107
 Klein, K. G., Verniero, J. L., Alterman, B., Bale, S., et al. 2021, *ApJ*, **909**, 7
 Kogan, V. I. 1961, in *Plasma Physics and the Problem of Controlled Thermonuclear Reactions*, ed. M. A. Leontovich (New York: Pergamon), 153
 Lazar, M., Poedts, S., & Fichtner, H. 2015, *A&A*, **582**, A124
 Li, X., & Habbal, S. R. 2000, *JGRA*, **105**, 27377
 López, R. A., Lazar, M., Shaaban, S. M., et al. 2019, *ApJL*, **873**, L20
 López, R. A., Micera, A., Lazar, M., et al. 2022, *ApJ*, **930**, 158
 López, R. A., Yoon, P. H., Viñas, A. F., & Lazar, M. 2023, *ApJ*, **954**, 191
 Maksimovic, M., Pierrard, V., & Lemaire, J. F. 1997, *A&A*, **324**, 725
 Maksimovic, M., Zouganelis, I., Chaufray, J.-Y., et al. 2005, *JGRA*, **110**, A09104
 Marsch, E. 2012, *SSRv*, **172**, 23
 Marsch, E., Ao, X. Z., & Tu, C. Y. 2004, *JGRA*, **109**, A04102
 Marsch, E., Zhao, L., & Tu, C.-Y. 2006, *AnGeo*, **24**, 2057
 Martinović, M. M., Klein, K. G., Đurovcová, T., & Alterman, B. L. 2021, *ApJ*, **923**, 116
 Maruca, B. A., Kasper, J. C., & Bale, S. D. 2011, *PhRvL*, **107**, 201101
 Maruca, B. A., Kasper, J. C., & Gary, S. P. 2012, *ApJ*, **748**, 137
 Matteini, L., Hellinger, P., Goldstein, B. E., et al. 2013, *JGR*, **118**, 2771
 Matteini, L., Landi, S., Hellinger, P., et al. 2007, *GeoRL*, **34**, L20105
 Mostafavi, P., Allen, R. C., Jagarlamudi, V. K., et al. 2024, *A&A*, **682**, A152
 Müller, D., St, Cyr, O. C., Zouganelis, I., et al. 2020, *A&A*, **642**, A1
 Noreen, N., Yoon, P. H., López, R. A., & Zaheer, S. 2017a, *JGRA*, **122**, 6978
 Opie, S., Verscharen, D., Chen, C. H. K., Owen, C. J., & Isenberg, P. A. 2022, *ApJ*, **941**, 176
 Perrone, D., Stansby, D., Horbury, T. S., & Matteini, L. 2019, *MNRAS*, **483**, 3730
 Pierrard, V., Lazar, M., Poedts, S., et al. 2016, *SoPh*, **291**, 2165
 Pierrard, V., Lazar, M., & Štverák, V. 2022, *FrASS*, **9**, 892236
 Pierrard, V., Maksimovic, M., & Lemaire, J. 1999, *JGR*, **104**, 17021
 Pilipp, W. G., Miggenrieder, H., Montgomery, M. D., et al. 1987a, *JGR*, **92**, 1075
 Pilipp, W. G., Miggenrieder, H., Montgomery, M. D., et al. 1987b, *JGR*, **92**, 1075
 Pilipp, W. G., Miggenrieder, H., Mühlhäuser, K.-H., et al. 1987, *JGR*, **92**, 1103
 Raouafi, N. E., Matteini, L., Squire, J., et al. 2023, *SSRv*, **219**, 8
 Rosenbauer, H., Schwenn, R., Marsch, E., et al. 1977, *JGZG*, **42**, 561
 Salem, C. S., Hubert, D., Lacombe, C., et al. 2003, *ApJ*, **585**, 1147
 Salem, C. S., Pulupa, M., Bale, S. D., & Verscharen, D. 2023, *A&A*, **675**, A16
 Sarfraz, M., López, R. A., Ahmed, S., & Yoon, P. H. 2022, *MNRAS*, **509**, 3764
 Sarfraz, M., Yoon, P. H., Saeed, S., Abbas, G., & Shah, H. A. 2017, *PhPI*, **24**, 021907
 Schwenn, R., Rosenbauer, H., & Miggenrieder, H. 1975, *RF*, **19**, 226
 Shaaban, S. M., Lazar, M., Poedts, S., & Elhanbaly, A. 2017, *Ap&SS*, **362**, 13
 Shaaban, S. M., Lazar, M., Yoon, P. H., & Poedts, S. 2019a, *A&A*, **627**, A76
 Shaaban, S. M., Lazar, M., Yoon, P. H., & Poedts, S. 2019b, *ApJ*, **871**, 237
 Sun, H., Zhao, J., Liu, W., Xie, H., & Wu, D. 2020, *ApJ*, **902**, 59
 Sun, H., Zhao, J., Xie, H., & Wu, D. 2019, *ApJ*, **884**, 44
 Štverák, Š., Maksimovic, M., Trávníček, P., et al. 2009, *JGRA*, **114**, A05104
 Štverák, Š., Trávníček, P., Maksimovic, M., et al. 2008, *JGRA*, **113**, A03103
 Štverák, Š., Trávníček, P. M., Hellinger, P., et al. 2015, *JGRA*, **120**, 8177
 Vafin, S., Riazantseva, M., & Pohl, M. 2019, *ApJL*, **871**, L11
 Vasyliunas, V. M. 1968, *JGR*, **73**, 2839
 Verscharen, D., Chandran, B. D. G., Boella, E., et al. 2022, *FrASS*, **9**, 951628
 Verscharen, D., Klein, K. G., & Maruca, B. A. 2019, *LRSP*, **16**, 5
 Wilson, L. B. I., Chen, L.-J., Wang, S., et al. 2019, *ApJS*, **243**, 8
 Wilson, L. B., III, Stevens, M. L., Kasper, J. C., et al. 2018, *ApJS*, **236**, 41
 Xiang, L., Lee, K. H., Wu, D. J., & Lee, L. C. 2020, *ApJ*, **899**, 61
 Xiang, L., Lee, K. H., Wu, D. J., Yu, H. W., & Lee, L. C. 2021, *ApJ*, **916**, 30
 Yoon, P. H. 2017, *RvMPP*, **1**, 4
 Yoon, P. H., Lazar, M., Salem, C., et al. 2024, *ApJ*, **969**, 77
 Yoon, P. H., López, R. A., Seough, J., & Sarfraz, M. 2017, *PhPI*, **24**, 112104
 Yoon, P. H., López, R. A., & Zaheer, S. 2023, *ApJ*, **950**, 131
 Zhao, G. Q., Li, H., Feng, H. Q., et al. 2019, *ApJ*, **884**, 60